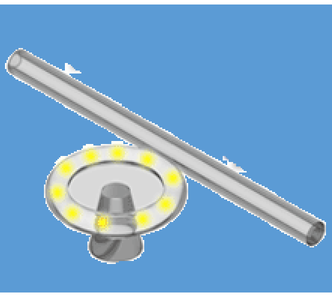

Annual report on research activities 2012

Keio University Faculty of Science and Technology

Tanabe Photonic Structure Group

Picture of lab members taken at Yagami campus on December 2012

Contents

Foreword 1

Lab Members 2

Research activity reports 3

“Revealing conditions required for achieving Kerr bistable memory based on whispering gallery mode cavity” 4

“Shape control of optical microcavities using crystal growth” 7

“Improvement of the laser reflow system and demonstration of resonant wavelength tuning by additional laser reflow” 10

“Study on the cell culture on the optical microcavity” 13

“Polygonal toroid microcavity for stable coupling with tapered fiber” 16

“Silica processing with semiconductor process” 19

“Study of detection of contamination of pure water using silica microspheres” 22

“Exploring high-Q/V mode using optimization algorithm” 25

Statistical data 28

Publications 29

Theses 30

The 13th Keio Techno-Mall 31

Foreword

I am much obligated to everyone who is supporting our group, in the department of Electronics and Electrical Engineering, in Keio University, Japan.

Year 2012 was the second year since we started our research activities in 2011. Now our team is with 10 students; 6 bachelors and 4 first-year master course students. Our group is studying the fundamental physics of light and trying to explore new applications of light. In particular we are interested in optical nonlinearities in microcavity systems.

Last year, we started our lab from scratch, where we constructed new measurement setups and wrote new program codes for simulation. With these tools, we could boost our research this year. In particularly, fabrication of a polygonal microcavity system and simulation on optical nonlinear memory in a silica microcavity system are the highlight of our group this year. These results have been published in journal papers, where the latter was selected as *Spotlight on Optics* in OSA journals.

We selected some of our research topics of this year, and put them together to make this report. All of the manuscripts are written by bachelors and first-year master course students. Therefore, I admit that some sentences are not well written. Even though, I am confident that the scientific contents provide important information and you may find interest in our research activities. I am appreciating and glad if you will give us any feedback to our researches.

August, 2013.
Takasumi Tanabe, Associate Professor,
Department of Electronics and Electrical Engineering,
Keio University

Lab Members (Names and their positions after graduation)

Assistant Professor

Takasumi Tanabe

Master 1st Grade:(The class of 2011)

Yohei Ogawa	Continues his education in the graduate school of Keio Univeristy
Takumi Kato	Continues his education in the graduate school of Keio Univeristy
Hiroshi Kudo	Continues his education in the graduate school of Keio Univeristy
Wataru Yoshiki	Continues his education in the graduate school of Keio Univeristy

Bachelor 4th Grade:(The class of 2012)

Kaho Ishikawa	Obtained the job after graduation
Ryusuke Saito	Continues his education in the graduate school of Keio Univeristy
Ryo Suzuki	Continues his education in the graduate school of Keio Univeristy
Tomohiro Tetsumoto	Continues his education in the graduate school of Keio Univeristy
Jiro Nishimura	Continues his education in the graduate school of Keio Univeristy
Akihiro Fushimi	Continues his education in the graduate school of Keio Univeristy

Research Activities

Revealing conditions required for achieving Kerr bistable memory based on whispering gallery mode cavity.

Wataru Yoshiki (M1)

This paper demonstrates that it is possible to obtain Kerr bistable memory in a whispering-gallery-mode cavity with an add-drop cavity system but it is impossible with a side-coupled cavity system when the thermo-optic effect is present.

Key words: Silica toroid microcavity; Optical bistability; Optical memory; Kerr effect; Coupled mode theory.

1. Introduction

Recent progress on the fabrication technology of ultra-high Q microcavities has enabled us to obtain an optical bistable memory with extremely low power [1, 2]. In our previous work [3], we demonstrated numerically that Kerr bistable memory operation is possible with a whispering-gallery mode cavity by choosing appropriate coupling with input/output waveguides and we used an add-drop system for that analysis. However, that study does not describe the quantitative conditions under which a Kerr bistable memory can be achieved.

Therefore, this paper reports that the quantitative conditions for achieving a Kerr bistable memory calculated by using a coupled mode theory-based numerical analysis. The analysis revealed that high-contrast operation can be obtained in an add-drop system but not in side-coupled system when the thermo-optic (TO) effect is present. The conditions clarified by the analysis are very important for achieving an optical Kerr bistable memory. .

2. Numerical model

This section describes the numerical model used for the analysis. We developed a numerical model of a side-coupled system (Fig. 1(a)) and an add-drop system (Fig. 1(b)), which consists of a silica toroid microcavity [4], by using the coupled mode theory (CMT) [5]. The master equations of the add-drop system are as follows;

$$P_{\mathrm{in}} = \tau_{\mathrm{coup1}}\left[\delta\omega(\Delta n)^2 + \frac{1}{4\tau_{\mathrm{loaded}}^2}\right]U_{\mathrm{cavity}} \qquad (1)$$

$$P_{\mathrm{out}} = \tau_{\mathrm{coup1}}\left[\delta\omega(\Delta n)^2 + \left(\frac{1}{2\tau_{\mathrm{loaded}}} - \frac{1}{\tau_{\mathrm{coup1}}}\right)^2\right]U_{\mathrm{cavity}} \qquad (2)$$

$$\delta\omega = 2\pi c\left[\frac{1}{\lambda_0(1+\Delta n/n_0)} - \frac{1}{\lambda}\right] \qquad (3)$$

Here U_{cavity}, P_{in}, P_{out}, c, λ_0, λ, n_0, τ_{loaded} and Δn are the light energy in the cavity, the input power, the output power, the light velocity, the resonant wavelength of a cavity, the input wavelength, the refractive index of the cavity, cavity loaded photon lifetime and the nonlinear refractive index change of the cavity, respectively. The loaded photon lifetime can be defined as $\tau_{\mathrm{loaded}}^{-1} = \tau_{\mathrm{int}}^{-1} + \tau_{\mathrm{coup1}}^{-1} + \tau_{\mathrm{coup2}}^{-1}$ where τ_{int} is the intrinsic photon lifetime and τ_{coup1} and τ_{coup2} are the photon lifetimes determined by the coupling with each waveguide. And the nonlinear refractive index change Δn is the sum of the refractive index change caused by Kerr and TO effect (Δn_{Kerr}, Δn_{TO}) as $\Delta n = \Delta n_{\mathrm{Kerr}} + \Delta n_{\mathrm{TO}}$. Note that if we apply Eqs. ((1)-((3) to a side-coupled system, we must simply to set τ_{coup2} as infinite.

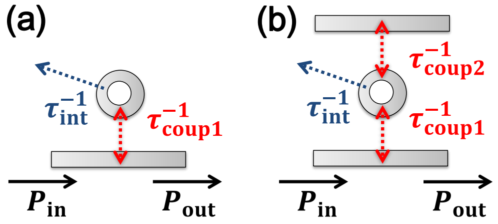

Fig. 1: (a) and (b): Models of side-coupled and add-drop system.

To achieve a Kerr bistable memory in an ultra-high Q cavity, we have to ensure that τ_{coup1} is small enough (corresponding to over-coupling between the cavity and the waveguide), because we have to finish the memory operation before the thermo-optic (TO) effect becomes dominant [3]. However, in a side-coupled system (Fig. 1(a)), a smaller τ_{coup1} results in shallower dips in the transmission spectra of the system, because the critical coupling condition ($\tau_{\mathrm{int}}^{-1} = \tau_{\mathrm{coup1}}^{-1}$) cannot be satisfied. As a result, it becomes difficult to discriminate between high and low output states, even though the cavity has two stable states for energy in the cavity. On the other hand, in an add-drop system (Fig. 1(b)), we can have a large contrast even when the coupling is very strong, because the critical coupling condition ($\tau_{\mathrm{coup1}}^{-1} = \tau_{\mathrm{int}}^{-1} + \tau_{\mathrm{coup2}}^{-1}$) can be satisfied by properly controlling $\tau_{\mathrm{coup1}}^{-1}$ and $\tau_{\mathrm{coup2}}^{-1}$. The use of an add-drop system is the key to achieve a Kerr bistable memory in the presence of the TO effect. To investigate this finding quantitatively, we have to obtain the data regarding the contrast between the two stable output states and the influence of the TO effect. Therefore, the remainder of this section explains how to calculate these data.

The contrast depends on the coupling strength (i.e. τ_{coup1} and τ_{coup2}) and the wavelength detuning $\delta\lambda = \lambda - \lambda_0$. With this in mind, we calculate the contrast for different τ_{coup1} and $\delta\lambda$ values by using Eqs. ((**1**)-((**3**) assuming an ideal condition where there is no nonlinear refractive index change other than the Kerr effect. An example the hysteresis curve for the light energy in a side-coupled system is shown by the blue line in Fig. 2(a) and (b). We can define the normalized contrast between two bistable output states $P_{\mathrm{out}}^{\mathrm{cont}} = \left(P_{\mathrm{out}}^{\mathrm{high}} - P_{\mathrm{out}}^{\mathrm{low}}\right)/P_{\mathrm{out}}^{\mathrm{high}}$ from Fig. 2(b). By repeatedly performing the calculations, we can obtain the contrast between the two stable output states $P_{\mathrm{out}}^{\mathrm{cont}}(\tau_{\mathrm{coup1}}, \delta\lambda)$ for given τ_{coup1} and $\delta\lambda$ values.

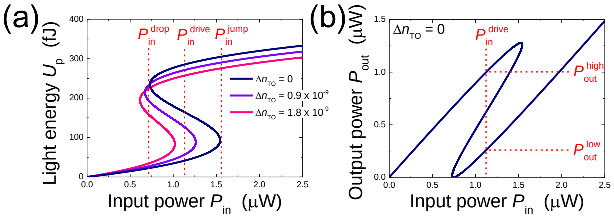

Fig. 2: Bistable behavior of a side-coupled system (a) the light energy U_{p} and (b) the output power P_{out} when $\tau_{\mathrm{coup1}} = \tau_{\mathrm{int}} = 329\ \mathrm{ns}$ and $\delta\lambda = 1.7 \times \Delta\lambda_{\mathrm{FWHM}} = 13\ \mathrm{fm}$.

Next, we analyze the influence of the TO effect. In general, the accumulation of heat makes it difficult to observe a Kerr bistable memory, so we should compare how large a TO effect is allowable for a Kerr bistable memory with how large a TO effect is induced. First, we focus on the former value. Since there is no carrier generation in a silica toroid microcavity, only TO (Δn_{TO}) and Kerr (Δn_{Kerr}) effects have to be considered. In an ideal case where the TO effect is negligible, the refractive index change Δn is equal to Δn_{Kerr} , and an ideal optical Kerr bistablity is obtained as shown by the blue line in Fig. 2(a). From this curve we can know the input drive power $P_{\mathrm{in}}^{\mathrm{drive}} = \left(P_{\mathrm{in}}^{\mathrm{jump}} + P_{\mathrm{in}}^{\mathrm{drop}}\right)/2$, which is required information if we are to use the system as a bistable memory. At the beginning of the memory operation, the memory can be operated according to the ideal curve because heat has not yet accumulated in the system. However, after a certain time, the accumulated heat becomes larger and Δn_{TO} is greatly increased. As a result, the curves gradually become deformed as shown by the purple and magenta lines in Fig. 2(a). Due to the deformation, there is only one output state in the magenta line on the input drive power $P_{\mathrm{in}}^{\mathrm{drive}}$. In general it is impossible to readjust $P_{\mathrm{in}}^{\mathrm{drive}}$ during operation, so we can no longer obtain a Kerr bistable memory when Δn_{TO} is very large. This is the difficulty involved in achieving a Kerr bistable memory in the presence of the TO effect. With this circumstance in mind, we investigated the maximum refractive index change caused by TO effect $\Delta n_{\mathrm{TO}}^{\mathrm{max}}$, which allows us to achieve a Kerr bistable stable memory by using Eqs. (1)-(3). The Kerr bistable memory only works while Δn_{TO} is smaller than $\Delta n_{\mathrm{TO}}^{\mathrm{max}}$.

Next, we estimate how much heat is accumulated during memory operation. As mentioned above, we can obtain an optical Kerr bistable memory only when $\Delta n_{\mathrm{TO}} \leq \Delta n_{\mathrm{TO}}^{\mathrm{max}}$. This means that when Δn_{TO} at the end of memory operation ($\Delta n_{\mathrm{TO}}^{\mathrm{end}}$) is smaller than $\Delta n_{\mathrm{TO}}^{\mathrm{max}}$, a Kerr bistable memory can be achieved without suffering from the TO effect during the entire operation. Therefore, we performed a transient CMT analysis, which is similar to the approach described in Ref. [3], to obtain $\Delta n_{\mathrm{TO}}^{\mathrm{end}}$ for different coupling τ_{coup1} and detuning $\delta\lambda$ values. The input waveform used in the calculation is shown in Fig. 3. Note that we normalize the time duration of the input waveform by each each loaded photon lifetimes (τ_{loaded}) because the response time of the cavity depends on its loaded photon lifetime. In our analysis, we employ $(a, b, c) = (20, 15, 25)$ (Fig. 3) and the set and reset pulse duration is 5.

By considering othe obtained $P_{\mathrm{out}}^{\mathrm{cont}}$, $\Delta n_{\mathrm{TO}}^{\mathrm{end}}$ and $\Delta n_{\mathrm{TO}}^{\mathrm{max}}$ for different τ_{coup1} and $\delta\lambda$ values, we can reveal the conditions that are necessary for achieving a Kerr bistable memory in the presence of the TO effect.

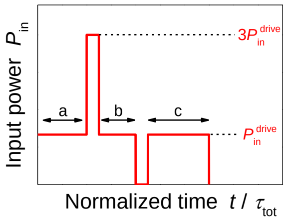

Fig. 3: The input waveform of the transient analysis. The time duration is normalized by the loaded photon lifetime τ_{loaded}. The power of the set pulse is $3P_{\mathrm{in}}^{\mathrm{drive}}$.

3. Results and discussion

Figure Fig. 4(a) and (b) show the results of numerical calculations both in a side-coupled system and an add-drop system. The color maps show the normalized contrast between the high and low states of the output power $P_{\mathrm{out}}^{\mathrm{cont}}$ for various τ_{coup1} and $\delta\lambda$ values when only Kerr nonlinearity is considered. Note that τ_{coup2} is properly controlled to satisfy the critical coupling condition ($\tau_{\mathrm{coup2}}^{-1} = \tau_{\mathrm{coup1}}^{-1} - \tau_{\mathrm{int}}^{-1}$) for an add-drop system (Fig. 4(b)). Fig. 4(a) indicates that the contrast disappears in a side-coupled system when τ_{coup1} is small because the critical coupling condition cannot be satisfied. On the other hand,

Fig. 4(b) shows that the contrast remained large even when τ_{coup1} was small in an add-drop system because the critical coupling condition can be satisfied by the appropriate control of τ_{coup2}.

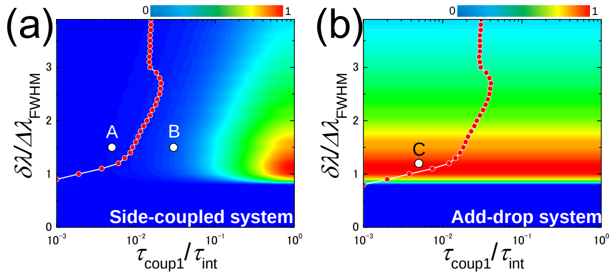

Fig. 4: $P_{\mathrm{out}}^{\mathrm{cont}}$ (color map) for different τ_{coup1} and $\delta\lambda$ values in (a) side-coupled system and (b) add-drop system. The x-axis and y-axis are τ_{coup1} and $\delta\lambda$ and normalized by τ_{int} and the full-width at half-maximum of the cavity resonance ($\Delta\lambda_{\mathrm{FWHM}}$), respectively. Note that points "A", "B" and "C" are placed on $(\tau_{\mathrm{coup1}}/\tau_{\mathrm{int}}, \delta\lambda/\Delta\lambda_{\mathrm{FWHM}}) = (0.005,1.5), (0.03,1.5)$ and $(0.005,1.2)$.

Red dots on the color maps indicate the conditions where $\Delta n_{\mathrm{TO}}^{\mathrm{end}}$ is equal to $\Delta n_{\mathrm{TO}}^{\mathrm{max}}$, which is obtained by the transient analysis. In the area to the left of the plots, $\Delta n_{\mathrm{TO}}^{\mathrm{end}}$ is smaller than $\Delta n_{\mathrm{TO}}^{\mathrm{max}}$, because the entire time required for the memory operation is shorter when τ_{coup1} (i.e. τ_{loaded}) is smaller, and a short memory operation time leads to a small-$\Delta n_{\mathrm{TO}}^{\mathrm{end}}$. This means that the Kerr effect can be used without it suffering from the TO effect when we perform a Kerr bistable memory operation under this condition. However, $P_{\mathrm{out}}^{\mathrm{cont}}$ is nearly zero in this small-τ_{coup1} area if we use a side-coupled system (Fig. Fig. 4(a)). As mentioned above, the bistable behavior cannot be observed if the contrast is small. Therefore we can conclude that optical bistable memory operation cannot be demonstrated with a side-coupled system in a realistic system where the TO effect is present. On the other hand, in the left area of the plots, $P_{\mathrm{out}}^{\mathrm{cont}}$ is very large in an add-drop system (Fig. Fig. 4(b)). This means that we can achieve a Kerr bistable memory by using an add-drop system.

To confirm whether the understandings obtained from Fig. 4 are really right or not, we conduct transient CMT analysis under the given conditions. Figure 5(a)-(c) show transient Kerr memory operations at points "A" and "B" shown in Fig. Fig. 4(a) and point "C" shown in Fig. Fig. 4(b). At point "A" (Fig. 5(a)), U_{cavity} shows a memory operation but P_{out} does not. This is because the critical coupling condition cannot be satisfied in a side-coupled system. Furthermore, neither U_{cavity} nor P_{out} show a memory operation at point "B" (Fig. 5(b)) because of the accumulation of heat. However both U_{cavity} and P_{out} clearly exhibit a memory operation at the point "C" (Fig. 5(c)) because the critical coupling is satisfied and the heat accumulation is very small under this condition. These results are almost same as those predicted by Fig. Fig. 4. Therefore, we can conclude that the use of an add-drop system and small τ_{coup1} are essential if we are to obtain a Kerr bistable memory in a realistic system where the TO effect is present.

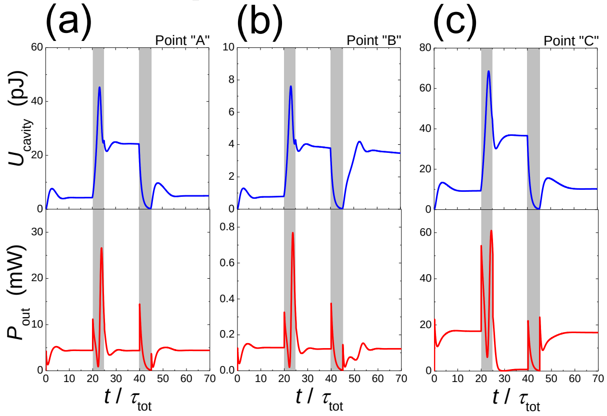

Fig. 5: Memory operation under point (a) "A", (b) "B" and (c) "C" conditions shown in Fig. 4. The blue and red solid lines represent the light energy and output power. The set/reset pulse is inputted in the gray zones.

4. Conclusion

In this study, we analyzed a Kerr bistable memory in both a side-coupled cavity system and an add-drop system. The analysis revealed that we must use an add-drop system and a short coupling photon lifetime if we are to achieve a Kerr bistable memory in the presence of the TO effect. In addition, we clarified the conditions under which a Kerr bistable memory can be achieved. These results are very important in terms of achieving a Kerr bistable memory not only in a silica toroid microcavity [1] but also ordinary WGM cavities [2].

References

[1] M. Yanik, *et al.*, Appl. Phys. Lett. **83**, 2739–2741 (2003).

[2] M. Pöllinger, *et al.*, Opt. Express **18**, 17764–17775 (2010).

[3] W. Yoshiki and T. Tanabe, J. Opt. Soc. Am. B **29**, 3335–3343 (2012).

[4] D. Armani, *et al.*, Nature **421**, 925–928 (2003).

[5] C. Manolatou, *et al.*, IEEE J. Quantum Electron. **35**, 1322–1331 (1999).

Shape control of optical microcavities using crystal growth

Hiroshi Kudo (M1) Ryo Suzuki (B4)

When we fabricate WGM microcavities by the laser-heated pedestal growth (LHPG) method, the crystalline makes the cavity configuration polygonal. Here I show that the shape can be controlled and changed from a hexagon to a circle. Also, I analyzed the dependence of Q on the curvature radius by numerical calculation. Furthermore, a circular microcavity achieved a Q of 16,000, which was higher than that of 8,500 obtained with a hexagonal cavity.

Key words: Crystal growth, Whispering gallery mode, Curvature radius, Crystalline

1. Introduction

The laser heated pedestal growth (LHPG) method is a technique applied for Czochralski method (CZ method), and it has been developed to realize a thinner, longer, and more uniform crystal fiber. [1] Crystal fibers are made by the procedure shown in Fig. 1. First, a feed rod is melted with a CO_2 laser or a YAG laser. Next, a seed rod is attached to the molten feed rod, and both are pulled upwards along the c-axis. Here, we can control the diameter of the grown rod by controlling the velocity ratio of the feed and the seed rods using Eq. 1. [2] The process described above is the standard LHPG method. Next, the velocity of the seed rod is reduced, and the rod is pulled away. Then, a bulge called a microcavity is formed, which can excite light. Here, v_1 is the velocity of the seed rod, v_2 is the velocity of the feed rod, v_1' is the velocity during microcavity fabrication, and τ is the duration of the microcavity fabrication.

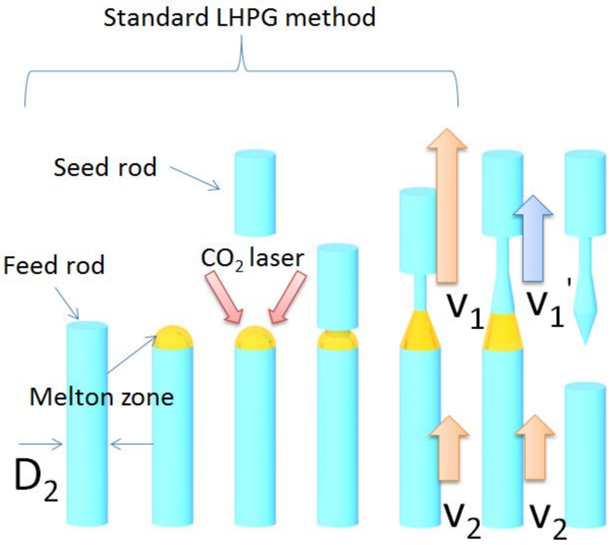

Fig. 1 Procedure for fabricating whispering gallery mode cavities using the LHPG method.

$$\frac{d_2}{d_1} = \frac{\sqrt{v_1}}{\sqrt{v_2}} \tag{1}$$

d_1: The dimeter of the feed rod
d_2: The dimeter of the seed rod
v_1: The velocity of the feed rod
v_2: The velocity of the seed rod

2. Fabrication result

Here, we fabricated a cavity where $v_1 = 12$ μm/s, $v_2 = 2$ μm/s, $v_1' = 6$ μm/s, and $\tau = 90$ sec.

Fig. 2 shows a cavity fabricated by using LHPG under the conditions described above. And, when we analyzed the TE mode by the finite element method we found that the cavity can excite light in a mode volume of 1.28×10^{-2} mm^3 according to Eq. 2.

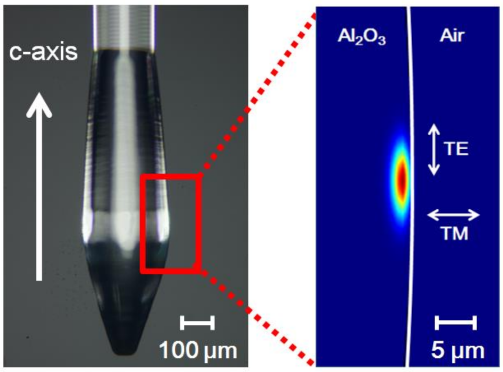

Fig. 2 WGM cavities fabricated using the LHPG method and the mode profile for the configuration. Here, the mode profile shows the TE mode for the configuration.

$$V_{\mathrm{mode}} = \frac{\iiint_{\mathrm{h,-s.}} \varepsilon |\mathbf{E}|^2 \mathrm{dV}}{\max[\varepsilon |\mathbf{E}|^2]} \tag{2}$$

ε: dielectric constant

3. Dependence of Q on curvature radius of polygonal cavities

The cavities fabricated by the LHPG method are polygonal because of the effect of crystalline shown in Fig. 3. The curvature radius of the polygonal configuration is thought to reduce the Q of the cavities because light is excited around the cavities in the whispering gallery mode. Therefore, we analyzed the dependence of Q on the curvature radius with a two-dimensional FDTD calculation. Here, the analysis was based on the model in the inset of Fig. 4. As a result, we found that Q increases as the curvature radius increases.

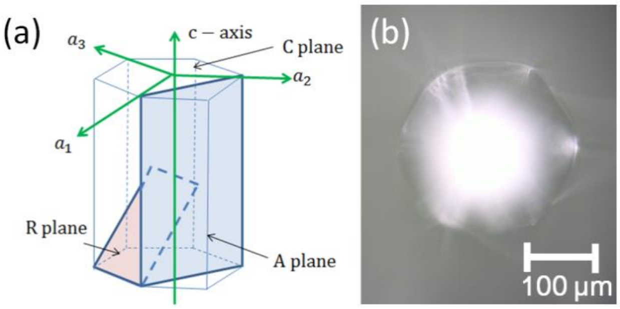

Fig. 3 (a) Crystalline plane of sapphire. (b) Microscope image of the cross-section of the microcavity fabricated by the LHPG method.

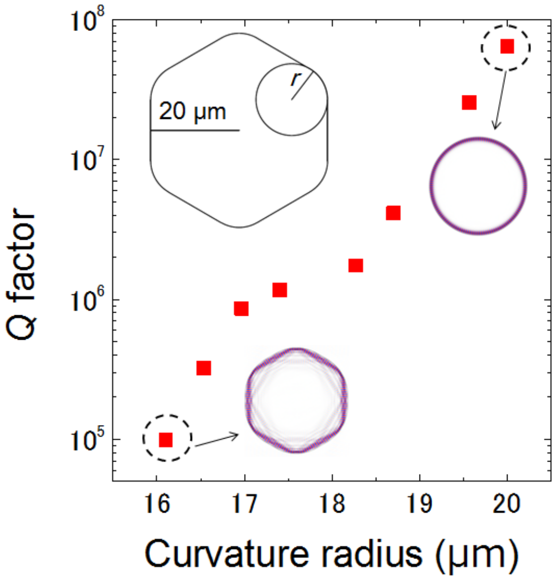

Fig. 4 Dependence of Q on the curvature radius of the hexagonal cavities. The inset in the upper left is the model used in the two-dimensional FDTD calculation. The other figures show the mode profile corresponding to each curvature radius.

4. Control of polygonal cavity configuration

As described in section 3, the cross-sectional configuration is hexagonal with the normal fabrication method. Here, we transformed the shape from a hexagon to a circle by preheating the seed rod before fabrication, as shown in Fig. 5(a). We call this process the "preheating method". Here we set L (the heated part of the seed rod) as a variable, as shown in the inset in Fig. 5. Fig. 6 (a) shows the change in the cavity shape from a hexagon to a circle. And, when L exceeds 8.0 mm, cracks occur in the grown part. Also, a comparison of the crystalline structure of a hexagonal cavity with that of a circular cavity reveals that both are single-crystalline, as shown in Fig. 6(b). However, there were higher order crystal planes in the crystalline structure of the circular cavity, which were caused by the deformation of the crystal plane.

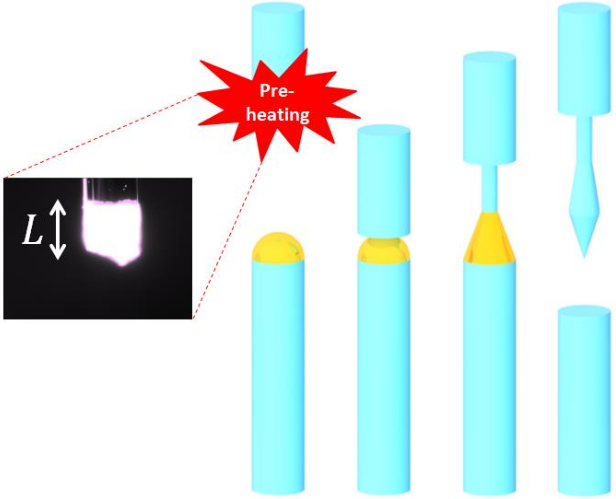

Fig. 5 Fabrication procedure with "pre-heating method". The inset is a CCD camera image obtained when the seed rod is heated before crystal growth.

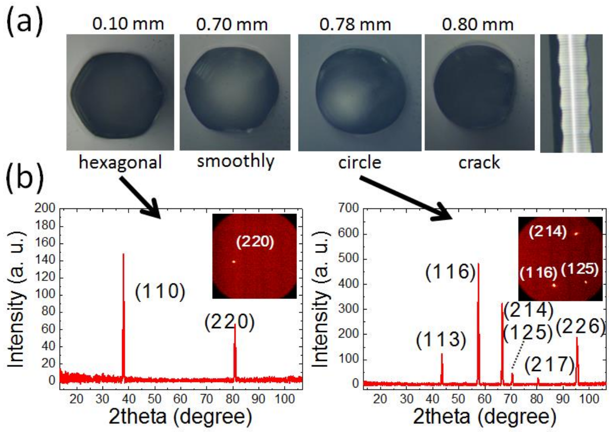

Fig. 6 (a) Microscope images of the change in the cross-sectional configuration according to L by the pre-heating method. When L exceeds 0.80 mm, cracks occur in the grown rod. (b) XRD analyses of the microcavities along the c-axis when L is 0.10 and 0.78 mm.

5. Improvement in Q by making the microcavities' shape rounder

We fabricated microcavities with hexagonal and circular shapes with the pre-heating method described in section 4. We then performed optical measurements on both cavities and compared the results, as shown in Fig. 7. We obtained a Q of 16,000 for a circular microcavity, and a Q of 8.500 for a hexagonal microcavity. In brief, we revealed experimentally that the Q of a polygonal cavity increases as the curvature radius increases, which is the same as the analysis result described in section 3.

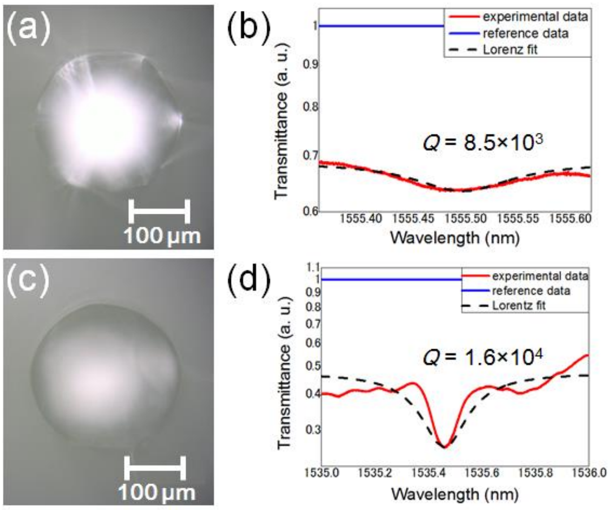

Fig. 7 (a) Microscope image of the cross-section of a hexagonal microcavity. (b) Optical measurement of a hexagonal microcavity. (c) Microscope image of the cross-section of a circular microcavity. (d) Optical measurement of a circular microcavity.

6. Conclusion

We showed that microcavities fabricated by the LHPG method have the ability to excite light in a mode volume of 1.28×10^{-2} mm^3. In addition, we analyzed the relationship between Q and the curvature radius of the microcavities using the two-dimensional FDTD method. As a result, we found that a rounder shape makes it easier to confine light efficiently in the WGM mode. And, we transformed the microcavity cross-section from a polygon to a circle using the pre-heating method. Finally, we demonstrated experimentally that the Q of a microcavity with a circular configuration is higher than that of a microcavity with a hexagonal configuration.

Acknowledgement

The author thanks Dr Atsushi Yokoo of NTT Basic Research Laboratories, NTT Corporation for useful discussions.

References

[1] A. Yokoo, S. Tomaru, I. Yokohama, H. Itoh, and T. Kaino, “A new growth method for long rod like organic nonlinear optical crystals with phase-matched direction” J. Cryst. Growth **156** 279-284 (1995).

[2] M. M. Fejer, J. L. Nightingale, G. A. Magal, and R. L. Byer, “Laser-heated miniature pedestal growth apparatus,” Rev. Sci. instrum. **55**, 11 (1984).

Improvement of the laser reflow system and demonstration of resonant wavelength tuning by additional laser reflow

Kaho Ishikawa (B4)   Wataru Yoshiki (M1)

In this research, we improved the laser reflow system used to perform the laser reflow processes of silica toroid microcavities. Furthermore, we confirmed the feasibility of resonant wavelength tuning by additional laser reflow. The observed resonant wavelength shift was approximately 100 pm toward blue wavelengths.

Key words: silica toroid micro cavity, laser reflow, CO_2 laser, wavelength tuning

1. Introduction

An optical microcavity is a small container that can confine light. The performance of a cavity can be evaluated in terms of its Q factor. A high Q cavity can greatly enhance the inner light intensity even when the power of the input light is very small.

A silica toroid microcavity was proposed in 2003 by Vahala’s group [1], The quality factor of this microcavity was 2.1×10^8 [1], which was much higher than that of a silicon micro-ring cavity ($Q = 1.43 \times 10^5$ [2]) or a photonic crystal cavity ($Q = 1.2 \times 10^6$ [3]).

Optical microcavities are expected to be used for cavity quantum electrodynamics (QED) or coupled resonator induced transparency (CRIT). Precise control of the resonant wavelength is very important if we are to employ microcavities for these applications; for example, the resonant wavelength of a cavity must be perfectly matched to the transition wavelength of a single atom in cavity QED experiments. However, since fabrication errors are inevitable, the resonant wavelength can differ from the designed wavelength. This makes cavity QED and CRIT difficult to achieve.

To solve this problem, a post-fabrication process has been commonly used that can tune the resonant wavelength. However, the post-fabrication wavelength tuning of an ultra-high Q cavity has not been reported. Therefore, in this research, we demonstrate the resonant wavelength tuning of a silica toroid microcavity by using an additional laser reflow process. Moreover, we also report an improvement of the laser reflow system that performs a preliminary procedure in wavelength tuning experiments.

2. Production process and post process

First, we describe the processes used to fabricate a silica toroid microcavity. A schematic diagram is shown in Fig. 1.

First, photolithography is employed on a silicon-on-insulator (SOI) substrate to create disk-shaped silica pads on silicon (top left in Fig. 1). Next, dry etching is carried out and the silica pads are undercut (top right in Fig. 1). Finally, the silica disk is irradiated with a CO_2 laser. Then, just the silica disk is melted and shrunk, and a mushroom-shaped structure (bottom of Fig. 1) is obtained because silica has a larger thermal conductivity and absorption coefficient than silicon. This process is called the "laser reflow process" and is essential if we are to achieve a silica toroid microcavity with an ultra-high Q.

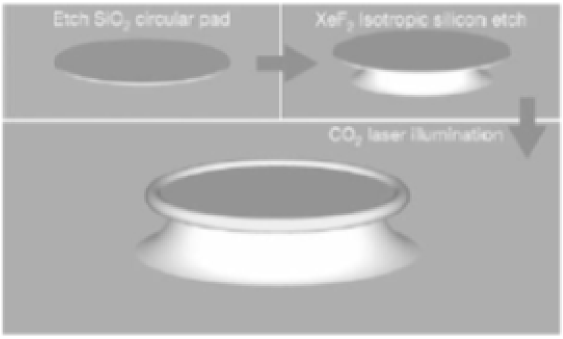

Fig. 1: Flow diagram illustrating the process used to fabricate silica toroid microcavities [1].

3. Improvement of laser reflow system

Next, we describe our improvement of the laser reflow system. Fig. 2 shows a silica toroid microcavity fabricated with the conventional system. When we employed the conventional system, the shape of the silica toroid microcavity became an ellipse. As a result of this distorted shape, the maximum Q was only about 10^{5}.

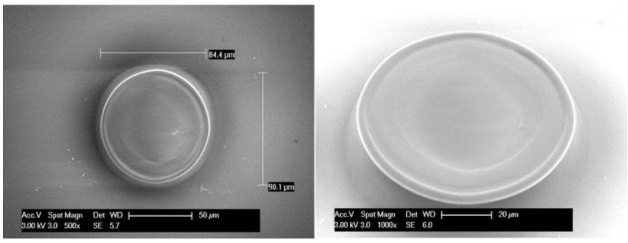

Fig.2: SEM picture of toroid microcavity fabricated with the conventional laser reflow system

We considered the cause of the distortion to be the fact that the beam spot provided by the lens was much smaller than the diameter of the disk. To make the beam spot larger, we replaced the lens of the reflow system with one that had a longer focal length. A schematic image is shown in Fig. 3.

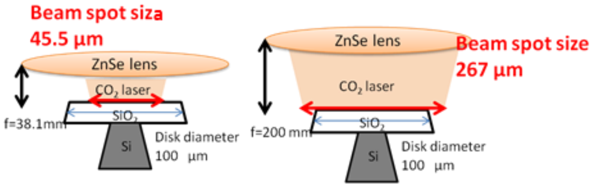

Fig. 3: Schematic configuration of beam spot.

Moreover, we improved the camera observation system. In the conventional system, we used a ZeSe lens that was designed to be used for IR light for both laser reflow and the camera observation system. This design made the camera resolution low and laser light alignment very difficult. To solve this problem, we employed a new objective lens, which was designed for use with visible light, for the camera observation system. The resolution of the camera improved and the laser light alignment became very easy. The new laser reflow system is illustrated in Fig. 4.

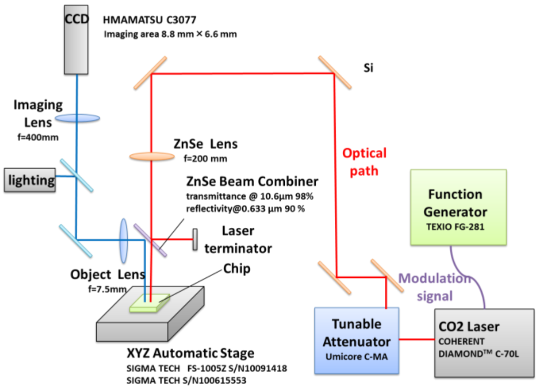

Fig. 4: Experimental set-up of the reflow process.

Fig. 5 shows scanning electron microscope (SEM) images of a silica toroid microcavity fabricated with the new laser reflow system. The laser irradiation power was 8 W (the power density was 104 MW/m^2) and the duration was 50 ms. The diameter was 90.16 µm and the edge was 2.63 µm thick. The *Q* of this cavity was 1.61×10^6, which is a significant improvement. On the other hand, this value is much lower than the *Q* of 1.25×10^8 reported in Ref. [1]. The *Q* of the fabricated cavity may be low because of surface roughness and a water layer on the surface. Therefore, we have to reconsider the irradiation power and duration of the laser reflow process to make the surface smooth. In addition we also have to prepare a N_2 purge system to prevent the water layer from forming on the surface.

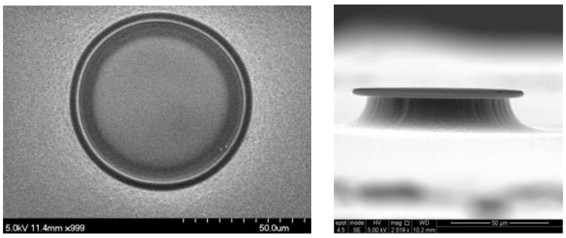

Fig.5: SEM image of toroid microcavity fabricated with the improved laser reflow system

4. Wavelength tuning with post process

The resonant wavelength of a silica toroid microcavity is denoted by the following equation.

$$m\lambda_{\mathrm{m}} = 2n\pi R, m = 1, 2, 3, \cdots \qquad (1)$$

According to Eq. (1), the resonant wavelength is proportional to the refractive index and radius of the cavity. Therefore, in this experiment, we conducted an additional laser reflow after the reflow process to reduce the cavity radius. As a result, we predicted that the resonant wavelength would be shifted. This is the principle behind our experiments.

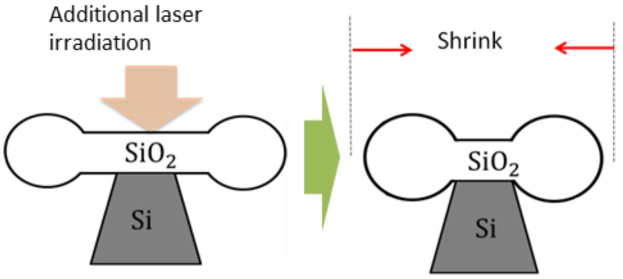

Fig. 6: Schematic tuning of SiO_2 toroid microcavities via additional laser irradiation. Before (left) after (right).

The procedure for the resonant wavelength tuning experiment was as follows.

【1】 We prepared several silica toroid microcavities on the same chip.

【2】 Measurement was started after 30 minutes to minimize the influence of TO and the formation of a water layer on the cavity surface (discussed later).

【3】 After measurement, the microcavities were reinstalled in the reflow system, and irradiated with the laser.

【4】 We performed procedures [2] and [3] repeatedly.

The toroid cavities were fabricated with an irradiation power of 4 W (power density 53.2 MW/m^2) and an irradiation duration of 50 ms. In the wavelength tuning experiments, the additional laser reflow power was gradually increased by 1 W, +2W, …, and 6 W. This is because the diameter of the toroid depends only on the laser reflow power [1], so we predicted that the diameter would not change if we performed an additional laser reflow with the same irradiation power.

Next, we report our experimental results. First, we show transmission spectra measured after the 1st and 2nd additional laser reflows (the irradiation powers were 1 and 2 W) in Fig. 7. The figure shows that the shape of the transmission spectra was greatly changed and the *Q* value was increased from 7.3×10^5 to 1.3×10^6 after the 2nd additional reflow.

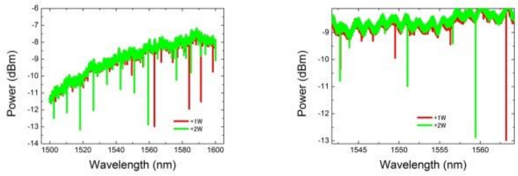

Fig. 7: Wavelength shift by additional 2 W irradiation power

The transmission spectra measured after the 2nd and 3rd additional laser reflows (the irradiation powers were 2 and 3 W) are shown in Fig. 8. The figure reveals a wavelength shift of 86 pm toward a shorter wavelength. After the 3rd additional reflow, the Q value decreased from 1.3×10^6 to 1.0×10^6.

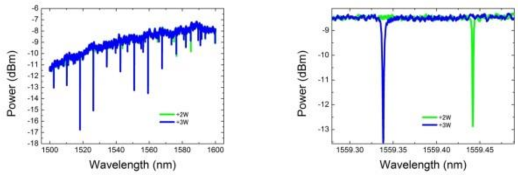

Fig. 8: Wavelength shift caused by additional 3 W irradiation power

The transmission spectra measured after the 5th and 6th additional laser reflows (the irradiation powers were 5 and 6 W) are shown in Fig. 9. The figure also shows that the shape was changed greatly after the 6th laser reflow as in Fig. 7. However, *Q* decreased from 6.7×10^5 to 6.2×10^4 in contrast to Fig. 7.

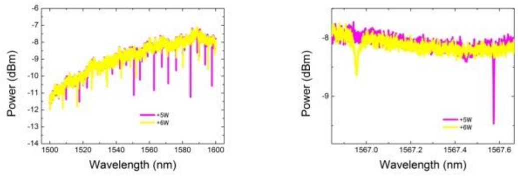

Fig. 9: Wavelength shift caused by additional 6 W irradiation power

Finally, we discuss the results. In Fig. 7 the shape of the transmission spectra was changed after the 2nd laser reflow. This is because the surface became smooth after the 2nd additional reflow and then high-*Q* resonance was generated. The increase in *Q* after the 2nd additional laser reflow supports this hypothesis.

Next, we discuss whether or not the wavelength shift in Fig. 8 is caused by the additional laser reflow. The resonant wavelength can be shifted for several reasons other than an additional laser reflow. These include the formation of a water layer on the surface, which can increase the cavity diameter, a thermo-optic (TO) effect and a change in the distance between a cavity and a taper, which can change effective refractive index of the cavity. However, we confirmed experimentally that the influence of the water layer and taper-cavity distance was trivial. In addition a wavelength shift of 100 pm corresponds to a temperature change of approximately 10K and it is unrealistic to regard that wavelength shift as being induced purely by a TO effect. Therefore, we can conclude that the wavelength shift was caused by the additional laser reflow.

Finally, we discuss the result shown in Fig. 9. We consider that the change in the transmission spectra was caused by the large diameter change. According to Eq. (1), a radius change of 1 μm leads to a wavelength shift of a few tens of nanometers. So it is very difficult to trace the wavelength shift when a high power additional reflow is irradiated. Note that the decreased *Q* was caused by the surface roughness induced by the high irradiation power.

5. Conclusion

In this study, we improved the laser reflow system and fabricated a silica toroid microcavity with a *Q* factor of 1.6×10^6, which is ten times higher than that of the cavity fabricated by the conventional system. Note that this value is much smaller than that reported in ref. [1] due to cavity contamination, surface roughness and water layer formation. The elimination of these effects is an important task.

Moreover, we achieved a resonant wavelength shift of about 100 pm by additional irradiation. When the irradiation power is too high, it is difficult to observe the wavelength shift because the induced wavelength shift is very large. We have not determined the optimum power yet and so we must conduct further experiments to examine the additional laser reflow conditions.

Reference

[1] D. Armani, T. Kippenberg, S. Spillane, and K. Vahala, "Ultra-high-*Q* toroid microcavity on a chip," Nature **421**, 925–928 (2003).

[2] Q. Xu, P. Dong, and M. Lipson, "Breaking the delay-bandwidth," Nat. Phys. **3**, 406–410 (2007)

[3] T. Tanabe, M. Notomi, E. Kuramochi, A. Shinya, and H. Taniyama, “Trapping and delaying photons for one nanosecond in an ultrasmall high-*Q* photonic-crystal nanocavity,” Nat. Photonics **1**, 49–52 (2007).

Study on cell culture in optical microcavity

Ryusuke Saito (B4)

The aim of this study is to analyze the 'cell cycle' with an optical microcavity. We must check whether a cell adheres to a silica microcavity, and then determine whether the cell is divided. NIH3T3 cells were placed in a microcavity and cultured, but the cells did not divide. When cells were added to the microcavity several times they adhered and cell division occurred.

Key words：silica optical microcavity, NIH3T3 cell, analysis cell cycle

1. Introduction

A cell cycle is defined as the period between cell divisions. In a cell cycle, cells compose chromosomes and distribute them equally between itself and its daughter cell. Until the early 20th century it was distinguished in a cell cycle solely from a resting stage and division stage or a division stage. In 1953, Haward and Pele discovered that DNA was synthesized during this specific interphase period. We divided a cell cycle into three phases called the G1 period, S period, and G2 period and established the concept of the cell cycle.

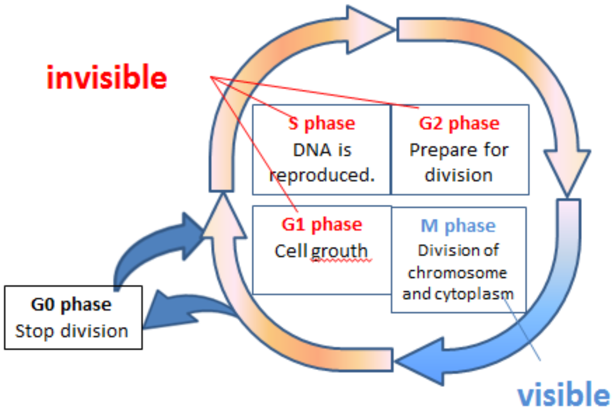

Fig. 1: Cell cycle. The M phase can be distinguished from the G1 phase or G2 phase using a microscope. But we cannot distinguish the G1, S and G2 phases.

Recently, cell cycle analysis has developed significantly, and we now know various things about the cell cycle at a molecular level. We showed that a cell develops and divides in different way depending on the influence of various external factors related to the particular organ and the individual. But we know little about how the progress of the cell cycle influences permeation or the metastasis of a morphosis and metastasize or infiltration of cancer. It is important that we understand when a cell cycle is controlled, or where a cell cycle is controlled. It is very important to both an understanding of basic biology and to cancer research to understand how a cell cycle is controlled. My aim is to examine the cell cycle analysis performed with fluorescence protein like Fucci technologies using a high *Q* silica optical microcavity, which is employed as a very highly sensitive sensor. We cannot ignore the secondary influence that a virus caused by the virus vector and the fluorescence protein itself has on a cell during analysis in a cell cycle using the fluorescence protein. When we undertake an analysis using a label free high *Q* silica microcavity, we can ignore other influences.

2. Examination of measurement in liquid

When we analyze a cell cycle using optical measurements, we must keep cell alive. Therefore, we must keep the cell in a medium. However, optical fiber is usually made with a suitable design in air so we must redesign it so that it is suitable for use in water, which has a higher absorption coefficient. The absorption loss of the light becomes small and so fiber diameter becomes large, but the light in the fiber must be single mode to achieve coupling between the optical fiber and the silica microcavity. The single mode condition in the stepped refractive index optical fiber can be expressed by the parameter V

$$V = 2.405 \tag{1}$$

We defined the refractive index of the fiber as $n_1 = 1.44$, and the refractive index of water as $n_2 = 1.33$, and then V can be written as below.

$$V = 2k_0 n_1 a\sqrt{2\Delta} \tag{2}$$

Therefore, for the single mode condition in the fiber in water, we defined a as fiber diameter

$$a < 2.15 \tag{3}$$

For the single mode condition in air, we defined the refractive index in air as $n_2' = 1$

$$a < 1.14 \tag{4}$$

If we reduce the absorption loss, we can satisfy the single mode condition. We must control the diameter by adjusting the pull time of the fiber to fabricate a $2\ \mu\mathrm{m}$ diameter fiber. Fig. 3 shows the relationship between fiber pulling time and diameter.

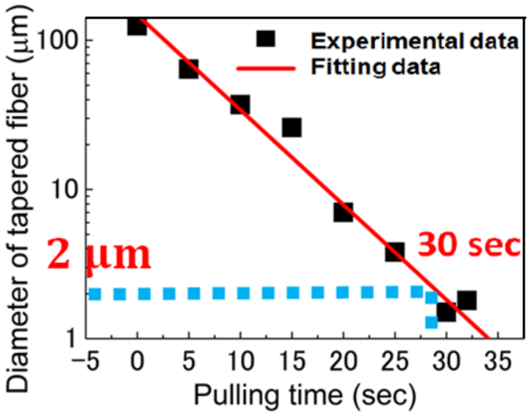

Fig. 2: The figure shows that we can make 2 µm diameter fiber if we continue to pull the fiber for about 30 seconds.

We fabricated fiber that met the water single mode condition, and Fig. 3 shows the measured transmissivity in air and in water.

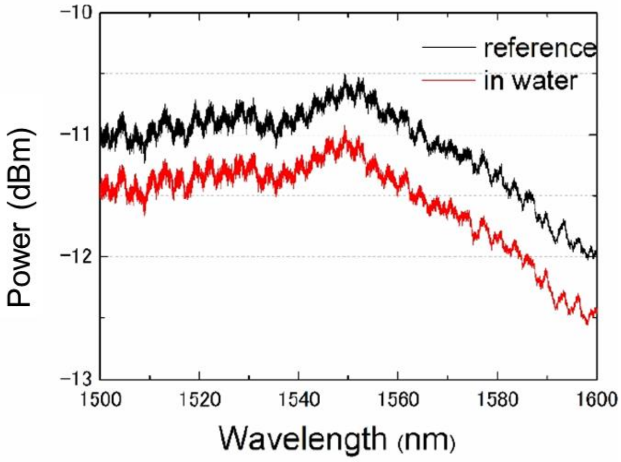

Fig. 3: This figure shows that suitable fiber was able to reduce the reduction in transmissivity to about 0.5 dBm in water, which has a higher absorption loss.

This result shows that this fiber is suitable for measurement in liquid, because we can reduce the absorption losses to -0.5 dBm. This means the output laser has 89% of the power of an input laser. We can measure the optical spectrum with small absorption losses in water using this fiber.

3. Experimental scattering of cells in microcavities

I performed the following procedures to scatter cells in an optical microcavity, and to culture cells.

I fabricated a silica tip with many silica microcavities, and soaked them in ethanol for more than 15 minutes to sterilize them. They were then irradiated with ultraviolet rays for more than 20 minutes.

1. I mixed the following medicines and prepared a nutrient medium.
   DMEM 45 ml
   PBS 5 ml
   Penicillin 1 ml
2. I prepared a dish with the following conditions and cultured a cell
   CO_2 density 5%
   Temperature 37℃
   Humidity 100%
3. I calculated the cell adhesion ratio and summarized it in the following notes.

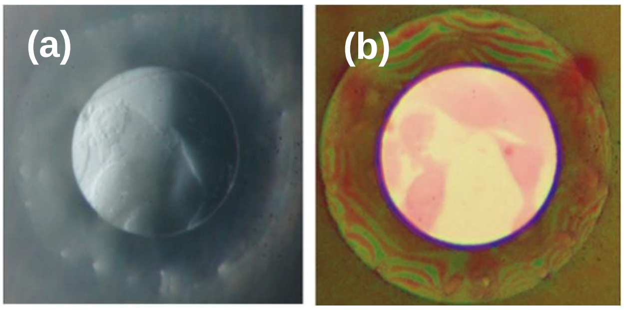

Fig. 4: (a) Cell that adhered to the microcavity. (b) Stained cell. We can determine that the semitransparent object is a cell.

Table 1

Microcavity	Number of microcavities	Microcavity with cells	Ratio
Disk	52	11	21.2
Toroid	51	2	3.92

Tab. 1 shows the ratio of success of the adherent cell. I fabricated about 100 microcavities. 52 silica disk microcavities and 51 silica toroidal microcavities. We can see only 11 silica disk microcavities with cells and 2 silica toroidal microcavities. I think it is more difficult for cells to adhere to the silica toroidal microcavity than to the silica disk microcavity.

Fig. 4 shows that this semitransparent object is actually a cell. However, almost every cell adheres alone as in Fig. 4 when I scatter cells in microcavities.

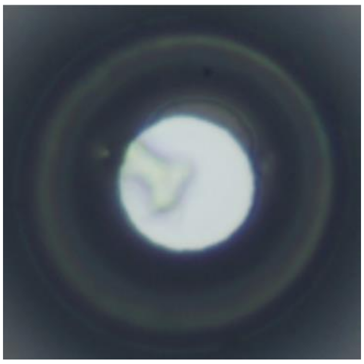

Fig. 5: Solitary cell. If I strew one time, the single cell adheres to the microcavity and it cannot split alone.

Because NIH3T3 is an adhesion-dependent cell, it must be divided. However, if it is alone the cell does not cause division even if it adheres to the tip. So, I carried out following experiment to induce cell division.

4. Experiment inducing cell division

A single cell does not induce cell division. Therefore, I carried out the following experiments, and I raised the density of the cell adhesion in an attempt to cause cell division.

1. I sterilized a tip with silica microcavities and placed a

cell on the tip.

2. I cultured the cell in an incubator for nine hours from eight hours and I removed the tip, observed the cell and placed cells on the tip once again.
3. I repeated the above experiment several times. I removed non-adhering cells and again supplied a nutrient medium, and I confirmed the adhesion of many cells.
4. I cultured the sample in an incubator for more than 24 hours.

I tested the sample in the above-mentioned procedure. The microcavity with many cells adhering to it is shown on the right in Fig. 6 and, the left figure shows cells that were cultured for more than 24 hours to cause them to divide.

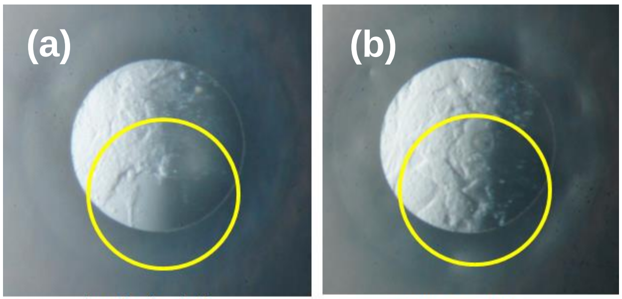

細胞分裂前　　細胞分裂後

Fig. 6: (a) shows a lot of cells adhering to the microcavity and (b) shows the cells can divide on the microcavity. The above experiment was effective in causing cell division.

We succeeded in inducing cell division on the silica microcavity and we connected this study with our last purpose of analyzing the cell cycle.

5. Conclusion

We spread NIH3T3 on a silica disk microcavity to analyze the label free cell cycle. We can affix more cells on a silica disk microcavity than on a silica toroidal microcavity. But we cannot observe cell division on the silica disk microcavity, so we disseminated many times and succeeded in observing cell division because many cells adhered to the microcavity. We will perform the same experiment on a silica toroidal microcavity with an ultra high Q factor to realize more delicate sensing.

5. References

[1] B. Alberts, A. Johnson, J. Lewis, M. Raff, K. Roberts, and P. Walter. “Molecular Biology of THE CELL Fifth Edition” Newton Press. (2009) (アルバート他，中村桂子，松原謙一他（訳）“THE CELL 細胞の分子生物学第5 版” ニュートンプレス) (2010).

[2] 國分泰雄，“光波工学” 協立出版株式会社，(1999).

[3] F. Vollmer and Stephen Arnold, “Whispering gallery mode biosensing: label-free detection down to single molecules” Nature Methods **5** 591-596 (2008).

[4] F. Vollmer, S. Arnold and D. Keng, “Single virus detection from the reactive shift of a whispering-gallery mode,” PNAS, **105**, 20701-20704 (2008).

Polygonal toroid microcavity for stable coupling with tapered fiber

Ryo Suzuki (B4)   Takumi Kato (M1)

To achieve robust optical coupling, we fabricated a polygonal silica toroid microcavity changing the fabrication process and evaluated the cavity performance theoretically and experimentally. Experimental results revealed that the optical characteristics were consistent with simulation results calculated using the FDTD method. In addition, a *Q* factor of 2.2×10^4 was recorded in contact with a tapered fiber.

Key words: Silica toroid microcavity, polygonal microcavity, evanescent field

1. Introduction

Various optical microcavities, which can confine light for a long time (high *Q* factor), have recently been proposed [1]. An ultrahigh-*Q* silica toroid microcavity is an ideal platform for demonstrating applications such as frequency comb generation, cavity QED, and highly sensitive biosensing [2]. The whispering-gallery mode (WGM) of the cavity is excited through an evanescent field with a tapered fiber. It is still a great challenge to use this cavity outside the laboratory for practical applications that require stable coupling because it requires fine (sub-μm order) control of the air gap. In this research, we show that stable coupling is possible even when the fiber is in contact with the cavity. And an octagonal silica toroid microcavity was fabricated by changing the fabrication process used for a circular toroid microcavity.

2. Fabrication of octagonal toroid microcavity

2.1 Anisotropic etching method

The silica toroid microcavity fabrication process has three steps, (1) photolithography, (2) silicon etching, and (3) laser reflow [2]. Fig. 1 shows steps (2) and (3). Circular toroid microcavity fabrication uses only isotropic etching (XeF_2) in (2). The addition of an anisotropic etching process (KOH), changes the toroid shape to an octagon, since the shape depends on the shape of the silicon post.

To consider the combination of isotropic and anisotropic etching, we established the optimum conditions for the process. Fig. 2 shows the fabricated result that we used for the optical measurement.

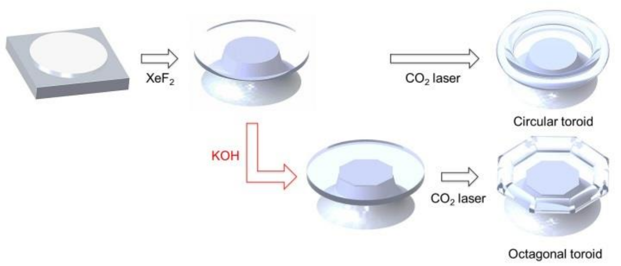

Fig. 1: Experimental fabrication process of circular and octagonal toroid microcavities. With the addition of a KOH etching process, the toroid becomes octagonal after the laser reflow.

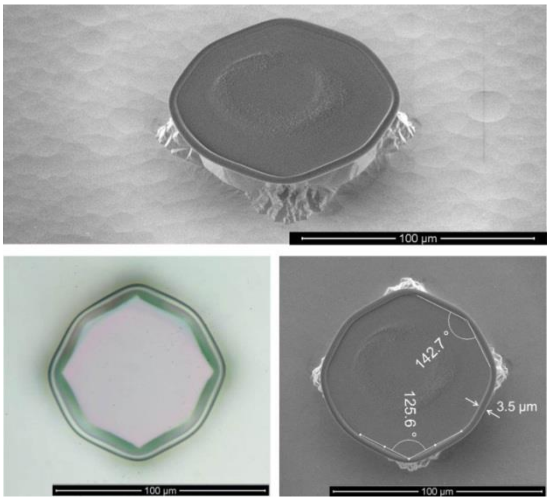

Fig. 2: Fabrication results of an octagonal silica toroid microcavity used for optical measurement.

2.2 Method of using octagonal silica disk

The fabrication of a polygonal toroid microcavity other than with an octagonal shape is impossible owing to characteristics of KOH (2.1). Accordingly, we fabricated an arbitrary silica disk by using photolithography to control the cavity shape. Fig. 3 (a) shows a regular octagonal silicon post after isotropic etching from an octagonal silica disk. The result after laser reflow in Fig. 3 (b) reveals that we can fabricate a desired shape such as a polygon, an ellipse and a circuit.

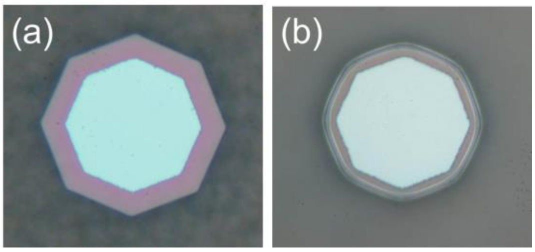

Fig. 3: Optical microscope images of a microcavity fabricated from an octagonal silica disk after (a) isotropic etching and (b) laser reflow.

3. Optical coupling with tapered fiber

The cavity mode is excited through an evanescent field with a tapered fiber about 1 μm in diameter. The effective Q factor (Q_{load}) is calculated from the intrinsic Q factor (Q_{unload}) and coupling loss (Q_{coup}).

Q_{load}: Effective Q factor (with coupler)
Q_{unload}: Intrinsic Q factor (without coupler)
Q_{coup}: Coupling loss

$$Q_{\mathrm{load}}^{-1} = Q_{\mathrm{unload}}^{-1} + Q_{\mathrm{coup}}^{-1} \tag{1}$$

Fig. 4 shows the relationship between coupling parameter κ, Q_{load} and transmittance T of the light propagating in the tapered fiber, when the air gap between the cavity and the fiber is decreasing gradually (increasing κ). The condition that achieves the most efficient optical coupling ($T = 0$) is called "critical coupling" [3]. To realize critical coupling with a circular toroid microcavity requires sub-μm order control. The purpose of this study is to attain critical coupling by changing a polygonal shape, even if the cavity is in contact with a tapered fiber.

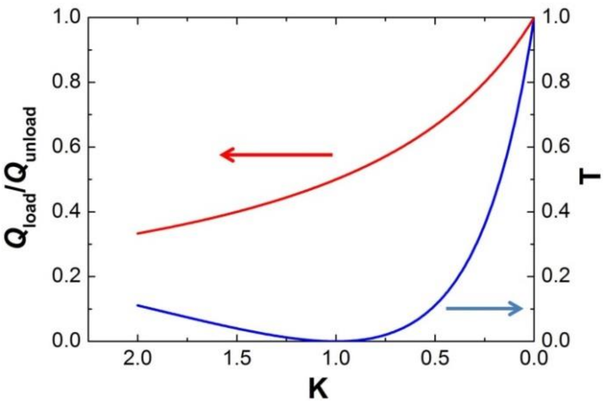

Fig. 4: Coupling parameter κ versus Q_{load} / Q_{unload} (red) and transmittance T (blue).

4. FDTD simulation

A simulation result calculated using the 2D-FDTD method is shown in Fig. 5 [4]. A close-up view of the cavity mode reveals that the light propagates close to the surface at the corner but slightly inward at the side. This small difference results in smaller coupling at the straight part and higher coupling at the corner. The Q factor is 8.8×10^{6} as calculated from the light intensity decay curve.

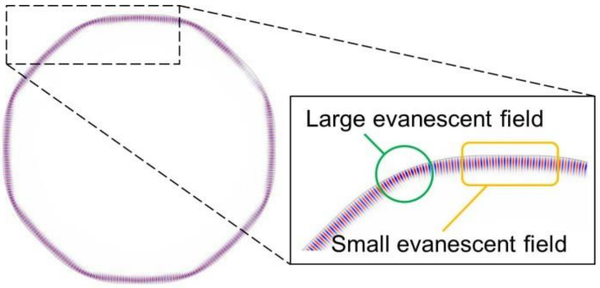

Fig. 5: Optical mode profile of an octagonal toroid microcavity calculated using the FDTD method. The inset shows a close-up view of the mode at the edge of the cavity.

5. Optical Measurement

We measured the transmittance spectrum of the octagonal cavity by using a standard tapered fiber setup and investigated the coupling coefficient. We placed the fiber at the side (parallel coupling) and at the corner (corner coupling) of the polygonal cavity and changed the air gap between the fiber and the cavity. Fig. 6 shows the dip depth of the resonance spectrum of the cavity with respect to the air gap. Since the depth is largest under the critical coupling condition, we can know from the graph that the fiber over-couples with the cavity when it is in contact with the corner of the cavity. On the other hand, it is close to the critical coupling condition when the fiber is in contact with the side of the cavity, and these results are in good agreement with the simulation results. The loaded Q factors were 2.2×10^{4} for parallel coupling and 6.3×10^{3} for corner coupling (both in contact) as shown in Fig. 7, and these values can be increased according to the calculation.

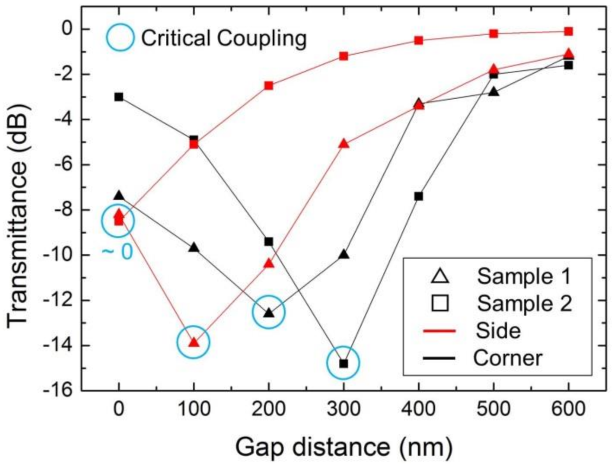

Fig. 6: Observation of critical coupling by measuring the transmittance vs air gap between the cavity and the tapered fiber.

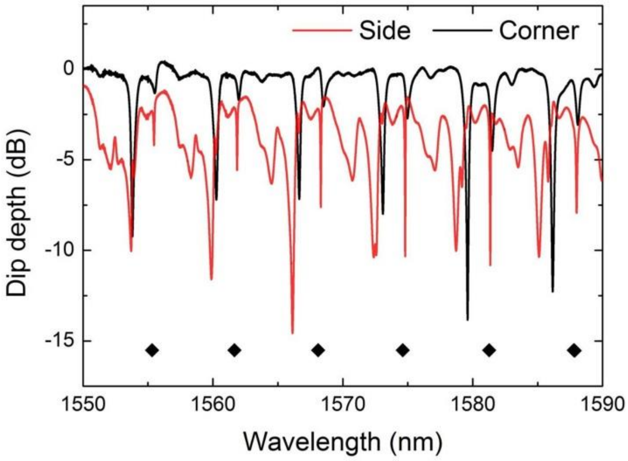

Fig. 7: Measured transmittance spectrum when a tapered fiber is in contact (air gap is 0 nm) at the side (red) and the corner (black) of the cavity. The dots represent the wavelength of the lowest order radial mode. The low background transmittance for the side coupling results from the excitation of the low-Q mode.

6. Conclusion

To achieve robust optical coupling with a tapered fiber, we evaluated an octagonal silica toroid microcavity. The cavity was fabricated by changing the condition of the photolithography or etching process. The experimental results reveal smaller coupling at the straight part and higher coupling at the corner. This agrees well with the result obtained by theoretical calculation. In addition, a *Q* factor of 2.2×10^4 was recorded in contact with a tapered fiber. We confirmed that various microcavity shapes such as polygons, ellipses and circuits can be fabricated. In summary, this is a step towards the demonstration of practical applications of toroid microcavities outside the laboratory because it offers the possibility of achieving stable coupling without requiring sub-μm alignment.

References

[1] K. J. Vahala, Nature **424** 839-846 (2003)
[2] D. K. Armani, T. J. Kippenberg, S. M. Spillane, and K. J. Vahala, Nature **421** 925-928 (2003).
[3] M. Cai, O. Painter, and K. J. Vahala, Phys. Rev. Lett. **85** 74-77 (2000).
[4] T. Kato, W. Yoshiki, R. Suzuki, and T. Tanabe, Appl. Phys. Lett. **101** 121101 (2012).

Silica processing with semiconductor process

Tomohiro Tetsumoto (B4)

Silica is transparent at telecommunication wavelengths and is a useful material for optical information technology. However, we have to develop advanced processing techniques to fabricate silica signal processing devices, because they require small and complicated structures. To obtain the necessary techniques for fabricating optical devices made of silica, we developed a semiconductor process recipe and fabricated a silica disk structure. In this work, we present the solution to technical challenges related to silica disk fabrication processes.

Key words: Silica; Photolithography; Silica toroid microcavity;

1. Introduction

A silica toroid microcavity has a very high quality factor and a superior capacity for integration on a chip, and so it has been used for many applications including optical switching, sensing and optomechanics. The cavity fabrication process is shown in Fig. 1. In this work, we fabricated a silica disk structure using semiconductor processes. First, we fabricated a photomask using laser lithography techniques. Next, we fabricated the silica disk structures by photolithography and dry etching. Finally, we fabricated a silica toroid microcavity and analyzed its optical properties. We also propose a solution for the problems that occurred during this fabrication process.

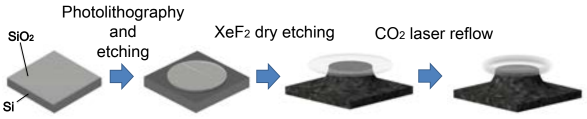

Fig. 1: Silica toroid microcavity fabrication process.

2. Photomask fabrication using laser lithography technique

Our laser lithography technique consists of the following three steps.

1. Preparing the CAD data of the mask pattern
2. Laser lithography
3. Developing and etching

The disk pattern of the previously used photomask was densely arranged. It made the depth of the undercut of a silica disk etched with XeF_2 gas uneven, and optical analysis difficult. So, first, we devised a CAD pattern to solve these problems. The CAD pattern is shown in Fig. 2. The disk patterns are arranged in columns and these columns are spaced with a sufficient distance. This pattern enables us to undertake XeF_2 dry etching uniformly and optical analysis easily. Also, we positioned an angular pattern, which is useful for focusing a CO_2 laser, at the end of each column, octagonal disks for use in fabricating the octagonal toroid cavity, and line structures to allow us to see the minimum line width of this process in the test pattern region.

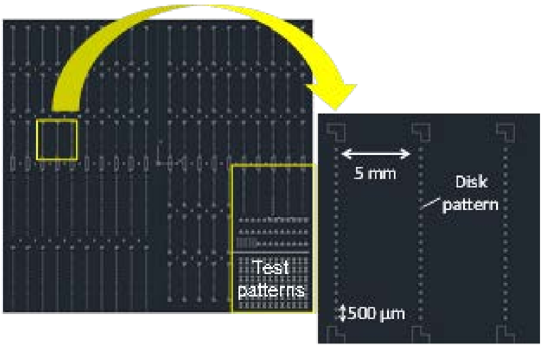

Fig. 2: CAD pattern of photomask.

Next, we formed the mask patterns with laser lithography. We used a DWL66fs (Heidelberg Instruments) equipped with a 365 nm Ar laser. We used a mask blank with a 540 nm photoresist layer of AZ 1350. After drawing the patterns, we developed the photoresist in AZ developer for 60 seconds, and a Cr layer was etched with Cr etchant.

The fabricated photomask is shown in Fig. 3 and its mask patterns are shown in Fig. 4. The disk patterns were fabricated well and the line structure was clearly formed up to 1.5 µm.

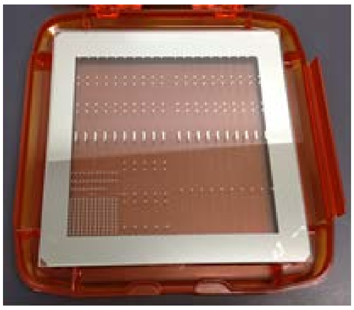

Fig. 3: Fabricated photomask.

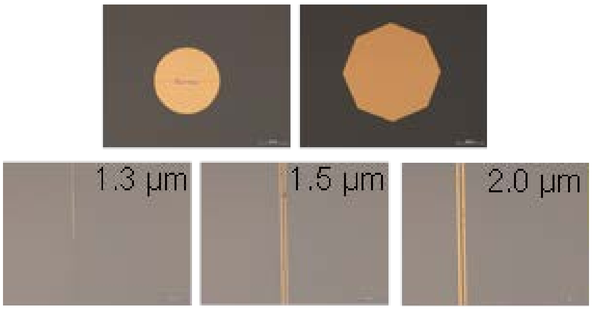

Fig. 4: Photomask patterns

3. Fabrication of silica disk by photolithography and dry etching

Photolithography is a precision processing method for fabricating semiconductors. The process consists of the following six steps (Fig. 5).

1. Preparing the wafer
2. Applying the photoresist to the wafer
3. Exposure
4. Developing the photoresist
5. Etching the silica
6. Removing the photoresist

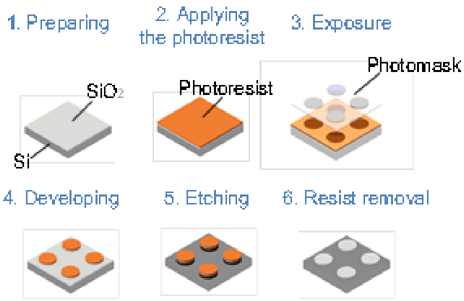

Fig. 5: Photomask patterns

We use OFPR 800LB (Tokyo Ohka Kogyo) as the photoresist, Gumma (Suss Micro Tech) as a coater and developer and MA6 (Suss Micro Tech) as the mask aligner for forming resist patterns. The recipe for forming the resist patterns is shown in Table 1.

Table 1: Photolithography recipe of OFPR 800LB.

Processes	Contents
Dehydration baking	110℃ 5 min
Vapor priming of HMDS	70℃ 15 sec (with HMDS vapor)
	70℃ 60 sec
Spin coating	300 rpm 3 sec
	1000 rpm 30 sec
	3000 rpm 2 sec
Pre-baking	110℃ 90 sec
Exposure	16.43 mW / cm^2 2.5 sec
Developing	20 rpm 5.5 sec (with TMAH)
	0 rpm 45 sec
	20 rpm 2 sec (Removing TMAH)
	20 rpm 5.5 sec (with TMAH)
	0 rpm 45 sec
	20 rpm 5.5 sec (Removing TMAH)
	20 rpm 5.5 sec (with TMAH)
	0 rpm 20 sec
Rinsing	1000 rpm, 15 sec (with hyperpure water)
	1500 rpm 15 sec (with N_2blowing)
	1500 rpm 30 sec, 3000 rpm 2 sec
Post-baking	120℃ 90 sec

The dry etching process was performed using an NLD-570 (ULVAC). This machine can make high-density plasma at low pressure when the magnetic field in the etching chamber is controlled. This enables us to fabricate fine high contrast structures. However, if we etch at high power, the photoresist turns hard and resist removal becomes very difficult especially in the edge region. A silica disk with residual photoresist at the edge is shown in Fig. 6. So, we optimized the etching recipe to make it possible to remove the photoresist easily with a remover. The optimized etching recipe is shown in Table 2. After etching, we removed the photoresist with AZ remover 700. The fabricated silica disk is shown in Fig. 7.

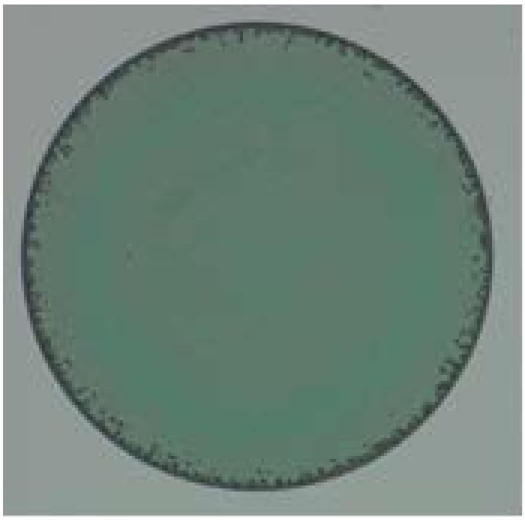

Fig. 6: Silica disk with residual photoresist.
It was etched with an antenna power of 1200 W and a bias power of 300 W.

Table 2: Etching recipe of silica disk.

Antenna power	300 W
Bias power	100 W
Etching gas	C_3F_8 10 sccm
Etching time	330 sec
Etching rate	190 nm / min

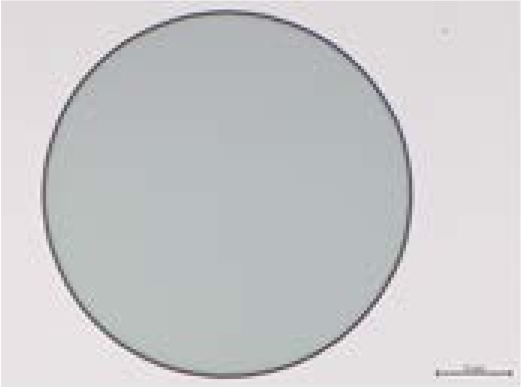

Fig. 7: Fabricated silica disk pattern.

4.   Analysis of silica toroid microcavity

We realized a silica toroid microcavity by applying XeF_2 etching and CO_2 laser reflow processes to the fabricated silica disk. A SEM image of the cavity is shown in Fig. 8. We also measured the transmission spectrum, and calculated the optical *Q* factor of the cavity. The results are shown in Figs. 9 and 10. The *Q* factor of the cavity was 1.3×10^6, and it was equivalent to the result obtained for the previous toroid cavity.

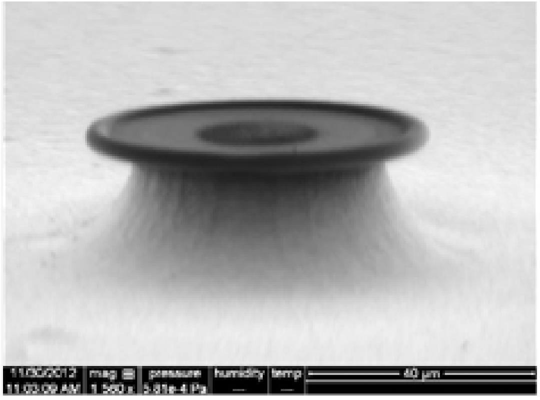

Fig. 8: SEM image of silica toroid microcavity.

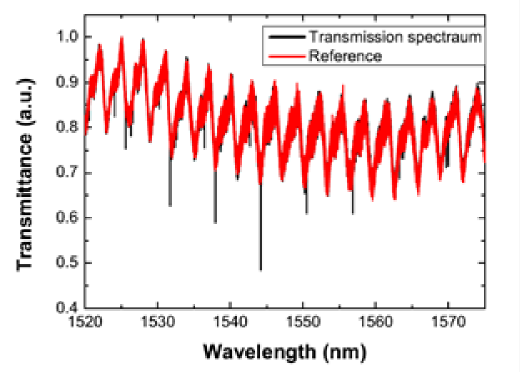

Fig. 9: Transmission spectrum of cavity.

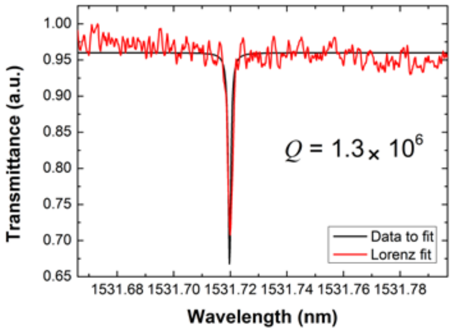

Fig. 10: Lorenz fitting of transmission spectrum.

5.   Conclusion

We developed a silica processing method by using semiconductor processing techniques and fabricated silica disk structures. We examined the problem of the residual resist caused by the etching conditions and proposed a solution. A silica toroid microcavity made from the silica disk showed an adequate level of performance.

6.   Facility

We used a clean room at Keio University and NANOBIC in Kawasaki City under the auspices of an academic consortium for nano and micro fabrication consisting of four universities.

References

[1] D. Armani, T. Kippenberg, S. Spillane, and K. Vahala, Nature **421**, 925–928 (2003).

[2] 山口宗弘, 半導体の製造工程(南日本新聞開発センター, 2003).

[3] 田邉功, 竹花洋一, 法元盛久, フォトマスク: 電子部品製造の基幹技術(東京電機大学出版局, 2011).

Study of detection of contamination of pure water using silica microspheres

Jiro Nishimura (B4)

We studied the detection of the contamination of pure water. We determined the relationship between the amount of resonant wavelength shift of silica microspheres and the quantity of ions in pure water. Using this principle, we studied the difference between the purities of pure water and city water.

Key words: Silica microsphere; Sensing; Resonant wavelength shift; Pure water.

1. Introduction

Recently, thanks to improvements in optical sensing technology, we can analyze molecular structures and detect molecular species and particles very sensitively. But with optical sensing there is a tradeoff between device size and sensitivity since sensitivity increases as the optical path length increases. This constraint can be overcome by using an optical microcavity, which provides a long optical path by confining the light. So, we can fabricate compact but highly sensitive optical devices. The use of an ultrahigh-Q microcavity with an 80 μm radius for 5×10^{-18} M IL-2 detection has already been reported [1].

We aim to fabricate a small and highly sensitive optical sensor using an optical microcavity. We studied the detection of the contamination of pure water using silica microspheres.

2. Sensing with optical microcavity

In optical sensing using an optical microcavity, we detect species and particles by measuring the amount of the resonant wavelength shift [2]. A resonant wavelength shift is caused by a change in the effective refractive index and optical path length of the cavity and this relationship is expressed by equation (1).

$$\frac{\Delta\lambda}{\lambda_0}=\frac{\Delta R}{R_0}+\frac{\Delta n}{n_0} \tag{1}$$

Where λ is the wavelength, R is the radius of the cavity and n is the refractive index. According to eq. (1), the greater the change in the effective refractive index and optical path length, the greater the resonant wavelength shift, and we can expect the resonant wavelength shifts of pure water and city water to differ. We studied the detection of the contamination of pure water by measuring the resonant wavelength shift.

3. Fabrication of silica microspheres

Our experimental setup is shown in Fig. 1. A light beam is formed into a doughnut shape by using two axicon lenses. By employing two gold mirrors, the beam is focused on the top of a single mode optical fiber. The top of the fiber is fused and becomes spherical as a result of surface tension. This is the process by which we fabricate silica microspheres. The size of the silica microspheres is roughly controlled by the radius of the fibers. Fig. 2(b) is an optical microscope image of a silica microsphere when a small radius fiber was used.

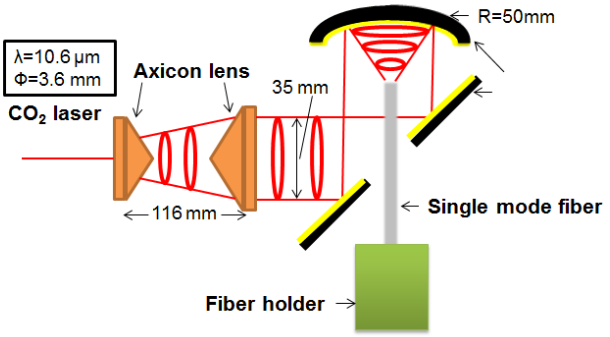

Fig. 1: Illustration of experimental setup for silica microsphere fabrication.

Fig. 2: Optical microscope images of silica microspheres.

4. Detection of contamination of pure water using silica microspheres

4.1. Relationship between the amount of resonant wavelength shift of silica microspheres and the quantity of impurities in pure water.

(1) Experimental method

1. Measure transmittance spectrum of silica microsphere after fabrication.
2. Soak microsphere in pure water or 0.005 M NaCl aq for 5 minutes.
3. Dry microsphere in a clean environment.
4. Measure transmittance spectrum of silica microsphere after the adsorption of liquid.

Fig. 3 shows the experimental process.

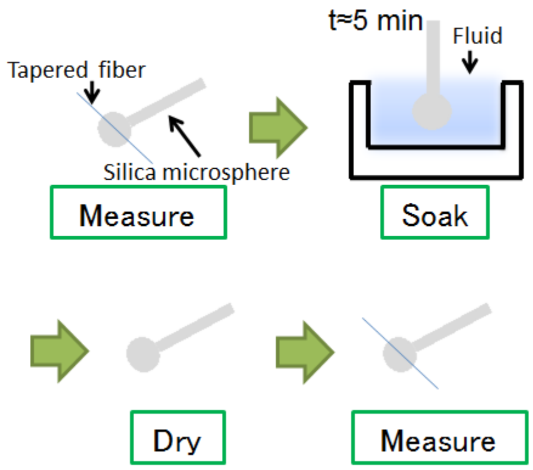

Fig. 3: Experimental process.

(2) Experimental result

Fig. 4(a), (b) show the resonant spectra obtained after the adsorption of pure water or NaCl aq. The result makes it clear that the resonant wavelength shift of NaCl aq is longer than that of pure water, and there is a relationship between the resonant wavelength shift of a silica microsphere and the quantity of impurities in pure water.

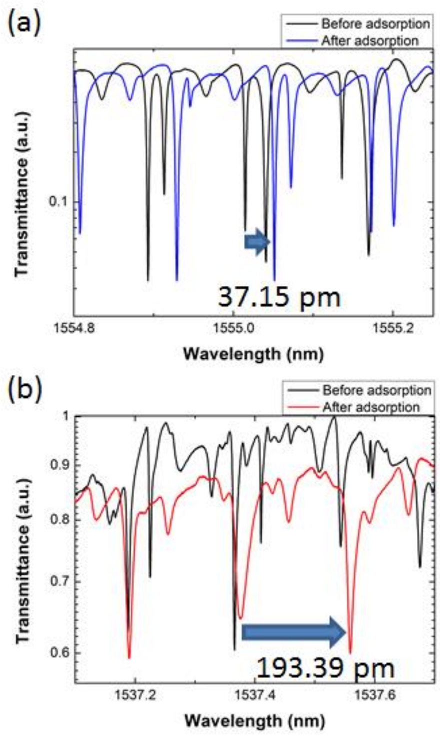

Fig. 4:(a) Resonant spectra of a silica microsphere. The black line is the spectrum after fabrication and the red line is after the adsorption of pure water. (b) The same as (a) before and after the adsorption of NaCl aq.

4.2. Detection of contamination of pure water.

(1) Experimental method

1. Measure transmittance spectrum of silica microsphere after fabrication.
2. Soak microsphere in pure water or city water for 5 minutes.
3. Dry microsphere in a clean environment.
4. Measure the transmittance spectrum of the silica microsphere after the adsorption of liquid.

(2) Experimental result

Fig. 5(a), (b) show the resonant spectra after the adsorption of pure water or city water. We performed the same experiment many times and obtained the histogram shown in Fig. 6. As seen in Fig. 6, the resonant wavelength shift was the same with pure water and city water. We investigate the causes below.

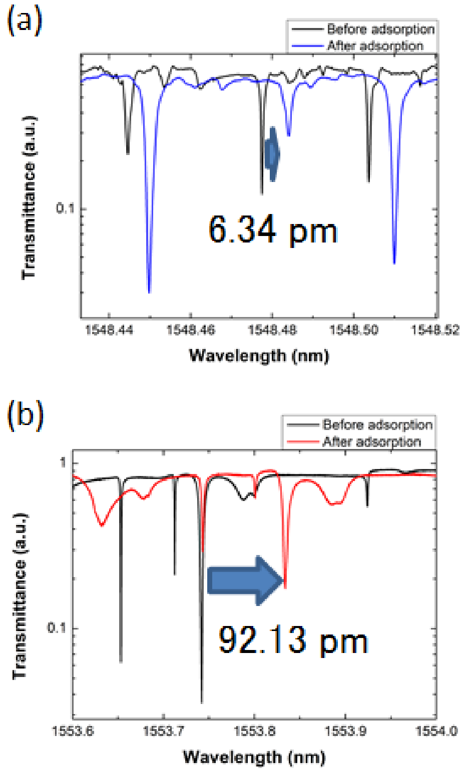

Fig. 5: (a) Resonant spectra of a silica microsphere. The black line is the spectrum after fabrication and the red line is after the adsorption of pure water. (b) The same as (a) before and after the adsorption of city water.

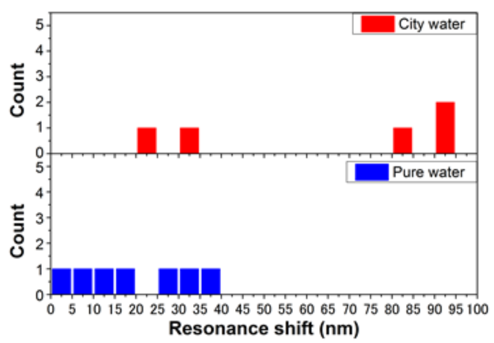

Fig. 6: Histogram of resonant shift.

(3) Study

We calculated Q_{abs}^{-1}, which represents the optical absorption by the particles on a microsphere, using equation (2) for pure water with a large shift, with a small shift and for city water.

$$Q_{ads}^{-1} = Q_{ori}^{-1} + Q_{abs}^{-1} \tag{2}$$

Here Q_{ads} is the *Q*-factor after adsorption, and Q_{ori} is that before adsorption. Q_{abs} was 10^5 for city water with a large shift, 10^6~10^7 for city water with small shift and 10^5~10^6 for pure water, and we assumed the following.

1. With city water, of the adsorption of the particle differed because of relationship between the resonant wavelength shift and Q_{abs}.
2. Despite the resonant wavelength shift being the same for pure water and city water, Q_{abs} is different, so pure water and city water react differently to silica.

(a) Difference in adsorption

We calculate ΔR, which indicates the change in the microsphere radius by equation below.

$$\frac{\Delta\lambda}{\lambda_0} = \frac{\Delta R}{R_0} \tag{3}$$

The vertical axis represents Q_{abs}^{-1} and the horizontal axis represents radius change. These two parameters generally have a proportional relationship, but this was not revealed by the result. So it is obvious that the difference in the adsorption is not the cause of the random shift. Its study constitutes future work.

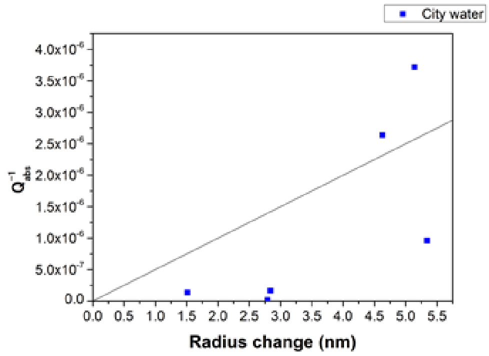

Fig. 7: Relationship between radius change and absorption loss.

(b) Difference in reaction to silica

We experimented as described below to study the difference in the reaction to silica.

1. Measure the transmittance spectrum of the silica microsphere after fabrication.
2. Soak it in city water for 5 minutes.
3. Dry it in a clean environment.
4. Measure the transmittance spectrum of the silica microsphere after the adsorption of city water.
5. Soak it in pure water for 5 minutes.
6. Dry it in a clean environment.
7. Measure the transmittance spectrum of the silica microsphere after the adsorption of city water.

Fig. 8 shows the resonant spectra we obtained after placing the microsphere in pure water followed by the adsorption of city water. Table 1 shows the *Q*-factor of the microsphere in each state. Even though the microsphere resonance wavelength became longer, it returned close to its original position after the microsphere had been exposed in pure water, which suggests that the particles on the microsphere surface were rinsed off. However, interestingly, the *Q*-factor continued to decrease even after the microsphere was placed in pure water. This indicates both that the attached particles were rinsed away, and that the surface of the microsphere itself is modified by the pure water. Since the wavelength is decreasing, we believe that the silica is reacting with water, as follows $SiO_2 + 2H_2O \rightarrow Si(OH)_4$.

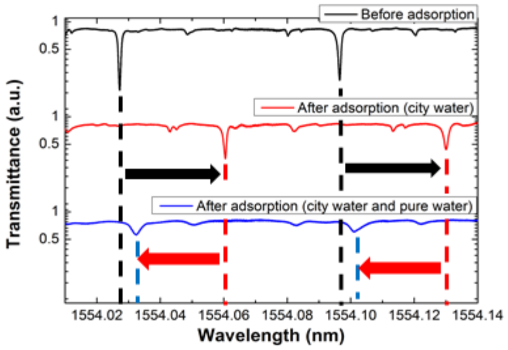

Fig. 8: Resonant spectrum before and after the cavity adsorbs city water or pure water.

Table 1: *Q*-factor of Fig. 8.

State	Q-factor
Before adsorption	1.31×10^6
After adsorption (city water)	1.28×10^6
After adsorption (city water and pure water)	4.19×10^5

5. Conclusion

We confirmed the relationship between the resonant wavelength shift and impurities. And we consider that pure water and city water react differently.

References

[1] A. M. Armani, R. P. Kulkarni, S. E. Fraser, R. C. Flagan, and K. J. Vahala, Science. **317** 783 (2007).

[2] F. Vollmer and S. Arnold, Nature Method **5** 591 (2008).

Exploring high-*Q*/*V* mode using optimization algorithm

Akihiro Fushimi (B4)

A mode profile with a Gaussian distribution experiences an ultrahigh *Q* in 2D photonic crystal nanocavities. We interpret the results of an optimization method and find a profile that has a smaller out-of-slab radiation than a Gaussian profile.

Key words: Photonic crystal; nanocavity; optimization; mode profile.

1. Introduction

Photonic crystal (PhC) offers good potential for use in constructing various photonic devices. However, we know only empirically that a mode profile with a Gaussian distribution has an ultrahigh *Q*.

We researched a profile with a smaller out-of-slab radiation than a Gaussian profile by using an optimization algorithm.

2. Momentum space analysis

The out-of-slab radiation losses in two-dimensional (2D) photonic crystal (PhC) nanocavities are the primary factors limiting the quality factor (*Q*) of the cavity. All of the light components in a nanocavity must satisfy total internal reflection to obtain an infinite *Q*. However, a leaky component called a light-cone (LC) component is always present. This is light that has an in-plane wave vector $|\mathbf{k}_{||}|$ at a value in the 0 and ω_0/c range (where ω_0 is the angular frequency, and c is the speed of light). It is known that a reduction of the LC component allows us to obtain an ultrahigh *Q* mode [1]. Since the spatial Fourier transformation (FT) of the in-plane electro-magnetic field distribution of a cavity mode gives the momentum distribution $|\mathbf{k}_{||}|$ for this mode, our task is to find the optimum spatial mode profile that allows as small an LC component as possible.

Currently, a mode profile with a Gaussian distribution is known empirically to exhibit the highest *Q* in a 2D PhC nanocavity [2]. Although a sinc distribution minimizes $|\mathbf{k}_{||}|$ in an LC, it is not a window function (i.e. not a function that has zero value outside the specified range) and the wave continues to infinity. Obviously we cannot design a resonator whose mode profile is exactly sinc. The purpose of this study is to clarify this theoretical problem and explore a mode profile (window function) that has a higher *Q* than a Gaussian profile by utilizing an optimization algorithm. An important part of such an optimization study is the interpretation of the results that are obtained. With this in mind, we employ different methods and try to understand the underlying physics from the final optimized profile.

Typically, the smaller the cavity mode volume *V* is, the lower the cavity *Q* becomes. Therefore, we optimized the mode profile with the condition that *V* remains the same during the optimization process. In addition, for simplicity, we start with a 1D problem and assume a uniform refractive index of n=3.45 (Fig.1). We used a simulated annealing (SA) method for the optimization. The cost function (figure of merit) that we used for the optimization is the sum of the momentum components (the total is normalized to 1) in an LC for a given spatial mode profile, because this causes out-of-slab radiation and this is what we want to reduce.

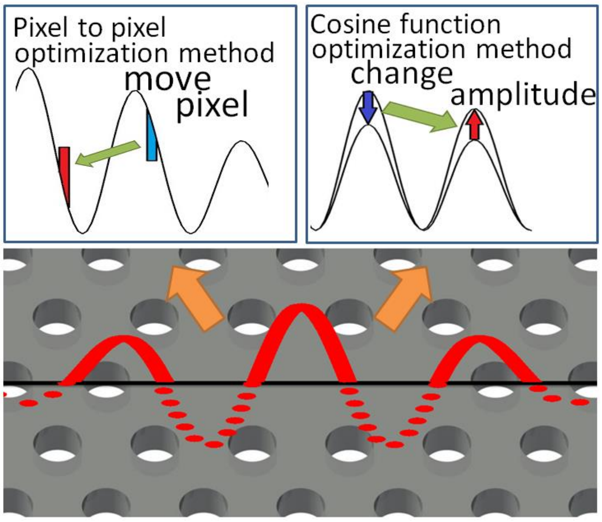

Fig. 1: Schematic illustration of the model and methods we used.

3. Pixel to pixel optimization method

We discretized the mode profile along the axial direction and performed pixel-by-pixel optimization. Namely, we randomly moved a part of the component to a different position and then calculated the cost. Figure 2(a) shows the initial and final electrical field distributions obtained by using this optimization method. The inset shows the cost, which has decreased almost two orders of magnitude. The optimized profile is quite different from a Gaussian profile, which has a sharp peak at the center and low amplitude at the side. The square waves are caused by the higher mode excitation, which we did not prohibit during the optimization. Other than that, the shape of the obtained profile appears similar to that of a slot cavity [3], which is known to have a high *Q*/*V*.

This result shows that the optimization method (along with careful interpretation) is a powerful tool for finding high *Q*/*V* profiles, such as a slot cavity in this case. Indeed, the cost of this profile is about half that of a Gaussian. However, such a profile with discontinuity is usually difficult to design, and we tried different methods to find a smooth profile with lower loss than a Gaussian.

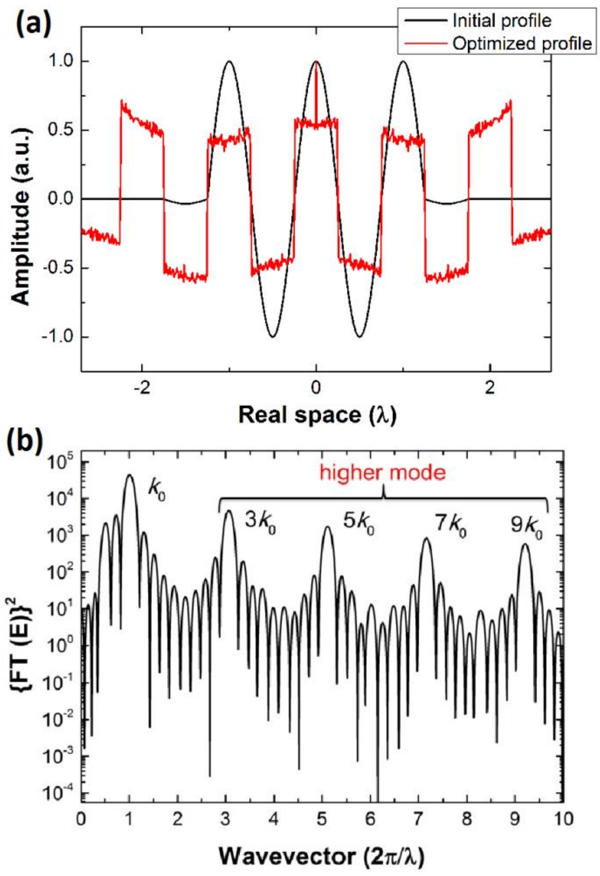

Fig. 2: (a) Result of pixel to pixel optimization method in real space. The black line is the optimized profile and the red line is the initial profile, which is set as a rect function. (b) Higher modes of the optimized profile obtained using pixel to pixel optimization method.

4. Cosine function optimization method

We changed the amplitude of each cosine wave as shown in Fig.1. This method precludes the excitation of higher modes, and enables us to search for a (global) minimum near the Gaussian profile. Initial and final profiles are shown in Fig. 3(a). The obtained shape is similar to a Gaussian profile, but the cost is smaller than that obtained with a Gaussian profile. With the help of the optimization algorithm we found that there is a profile that has a higher *Q* than a Gaussian distribution. In addition, a careful comparison of Fig. 3(a) and a Gauss function revealed that the profile of the optimized mode has more components at the center and is sharper in the tails than a Gaussian profile.

5. Exponential power distribution

Based on this observation, we employed an exponential power distribution defined as

$$p(x) = \exp\left\{-\left(\frac{|x|}{w}\right)^{\alpha}\right\} \tag{2}$$

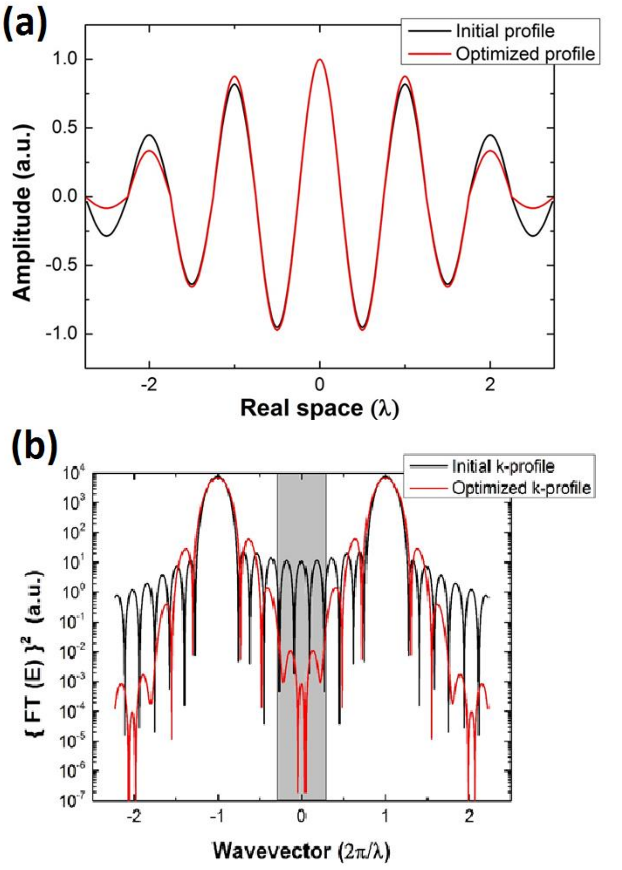

Fig. 3: (a) Result of amplitude optimization method in real space. The black line is the optimized profile and the red line is the initial profile, which is set as a Gaussian profile. (b) Result of amplitude optimization method in k space. The black line is the optimized profile and the red line is the initial profile. The gray area indicates the light line.

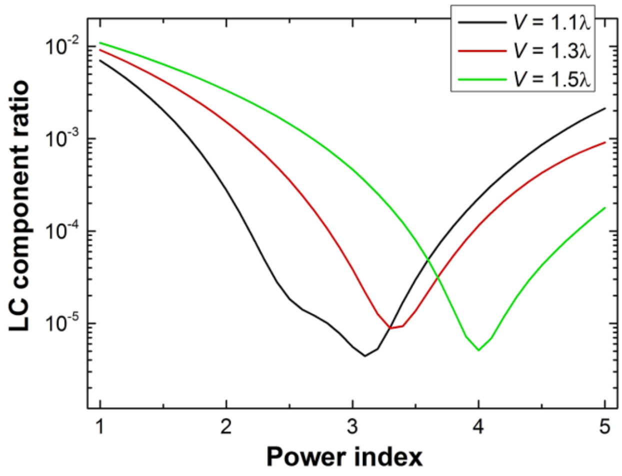

Fig. 4: LL component ratio vs power index for the difference of mode volume.

, which includes a Gaussian when α=2. When α is large, the spatial light components gather at its center, which we expect to explain the result in Fig. 3(a). Finally, we investigated the cost in function to α for different *V*s as shown in Fig. 4. The graphs show that the cost is minimum at different α values when we change *V* (i.e. α =3.3 for *V* =1.3λ). It is noteworthy that the cost at the optimum α is a few orders smaller than that of a Gaussian profile.

6. Conclusion

We obtained a profile of the optimized mode that has more components at the center and sharper tails than a Gaussian profile by using an optimization algorithm that is the sum of the momentum components in an LC. Based on this observation, we employed an exponential power distribution. The optimized power index α depends on the mode volume V.

References

[1] K. Srinivasan and O. Painter, Opt. Express **10** 670 (2002).
[2] Y. Akahane, T. Asano, B. Song, and S. Noda, Nature **425** 944 (2003).
[3] J. Robinson, C. Manolatou, L. Chen, and M. Lipson, Phys. Rev. Lett. **95** 143901 (2005).

Statistical Data

Publications

(April 2012-March 2013)

Journal Papers:

[1] T. Kato, W. Yoshiki, R. Suzuki, and T. Tanabe, "Octagonal silica toroidal microcavity for controlled optical coupling," Appl. Phys. Lett., Vol. 101, 121101 (2012).

[2] W.Yoshiki and T.Tanabe, “Analysis of bistable memory in silica toroid microcavity” J. Opt. Soc. Amer. B, Vol. 29, No. 12, pp. 3335-3343 (2012).

International Conferences:

[1] W. Yoshiki and T. Tanabe, “Rigorous analysis of bistable memory in silica toroid microcavity,” Conference on Lasers and Electro-Optics and International Quantum Electronics Conference (CLEO2012), CM2M.8, San Jose, May 6-11 (2012).

[2] H. Kudo, Y. Ogawa, T. Tanabe, and A. Yokoo, “Fabrication of whispering gallery mode cavities using crystal,” Fifth International Conference on Optical, Optoelectronic and Photonic Materials and Applications (ICOOPMA12), 1253, Nara, June 3-7 (2012)

[3] T. Kato, W. Yoshiki, Y. Ogawa, and T. Tanabe, " Polygonal silica toroidal microcavity for easy and stable coupling with waveguides," 2012 Frontiers in Optics/Laser Science XXVIII meeting (FiO/LS), FTu4A.5, Rochester, October 14-18 (2012).

[4] H. Kudo, Y. Ogawa, T. Tanabe, and A. Yokoo, "Crystalline whispering gallery mode cavities directly fabricated by crystal growth," 2012 Frontiers in Optics/Laser Science XXVIII meeting (FiO/LS), FTh1G.6, Rochester, October 14-18 (2012).

[5] W. Yoshiki and T. Tanabe, "Analysis of four-port system for bistable memory in silica toroid microcavity," 2nd International Symposium on Photonics and Electronics Convergence (ISPEC 2012), C-4, Tokyo, December 3-5 (2012).

Theses

Bachelor Theses

Kaho Ishikawa “Improvement of the laser reflow system and demonstration of resonant wavelength tuning by additional laser reflow”

Ryusuke Saito “Study on the cell culture on the optical microcavity”

Ryo Suzuki “Polygonal toroid microcavity for stable coupling with tapered fiber”

Tomohiro Tetsumoto “Silica processing with semiconductor process”

Jiro Nishimura “Study of detection of contamination of pure water using silica microspheres”

Akihiro Fushimi “Exploring high-Q/V mode using optimization algorithm”

The 13th Keio Techno-Mall

We had an exhibition booth and a poster presentation presenting our research activities in Keio Techno-Mall at Tokyo International Forum on 7th December 2012.   At the exhibition booth, we presented recent research results funded by grant-in-aid on the Next Generation Research Project in Keio University.   It is a collaborated project by three groups; Tanabe’s (EEE), Kakinuma’s (SD), and Terakawa’s (EEE) groups.